



## Constraining the terminal Ediacaran seawater chemistry by Mg isotopes in dolostones from the Yangtze Platform, South China

Pan Zhang <sup>a</sup>, Kang-Jun Huang <sup>a,\*</sup>, Mao Luo <sup>b,\*</sup>, Yaoping Cai <sup>a</sup>, Zhian Bao <sup>a</sup>

<sup>a</sup> State Key Laboratory of Continental Dynamics, Shaanxi Key Laboratory of Early Life and Environment, and Department of Geology, Northwest University, Xi'an 710069, China

<sup>b</sup> State Key Laboratory of Palaeobiology and Stratigraphy, Nanjing Institute of Geology and Palaeontology and Center for Excellence in Life and Palaeoenvironment, Chinese Academy of Sciences, 39 East Beijing Road, Nanjing 210008, China

### ARTICLE INFO

**Keywords:**  
Ediacaran  
Animal biomineralization  
Dolomite cement  
Seawater chemistry  
Mg isotopes

### ABSTRACT

The advent of animal biomineralization at the terminal Ediacaran remarkably changed the marine ecological system. Changed seawater Mg/Ca ratio is considered as an important external trigger for this transition, but the intrinsic relationship between seawater Mg/Ca variation and animal biomineralization is not well constrained due to the lack of reliable archives. To constrain the coeval seawater chemistry and explore its role in the origin of metazoan biomineralization, we systematically conducted petrographical and geochemical investigations on dolostones from the terminal Ediacaran (~551 Ma) Dengying Formation of the Yangtze Block in South China. The well-preserved sedimentary fabrics, growth zones as well as cathodoluminescent bands in microbialites and fibrous dolomite cements in the Algal Dolomite Member of the Dengying Formation indicate these dolomites were formed during syn-sedimentary diagenesis. The distribution patterns of rare earth elements in these dolomite components documented relatively anoxic shallow water conditions. Furthermore, negative correlations between O and Mg isotope compositions in well-preserved dolomite components indicate the variable mixture of freshwater with seawater in the shallow platform environment. The pervasive influence of freshwater on seawater indicates an enhanced riverine input, and it should be dominated by silicate weathering flux due to the heavier Mg isotopic compositions in freshwater endmember. Enhanced silicate weathering flux at the basal Dengying Formation may be related to the abundant erosions and exposures caused by the significant changes in Earth's surface tectonic and climatic conditions at the late Ediacaran. Consequently, the increased silicate weathering flux would deliver more Mg cations and net alkalinity to the oceans than the mixed weathering flux, which probably facilitated the subsequent skeletonization of early animals.

### 1. Introduction

The first appearance of protective skeletons in macro-metazoans can be traced to the late Ediacaran (Knoll, 2003; Wood et al., 2017a). The advent of such widespread mineralized skeleton in metazoans is not only accounted as a potential driver for the explosive increase in animal diversity, but also responsible for the enhanced ecosystem complexity and marine sediment production (Wood, 2018; Murdock, 2020). The potential external triggers of this innovation in early animals are diverse, and changes in marine environmental contexts, including marine redox, carbonate supersaturation, alkalinity, Mg/Ca ratio, and nutrient supply (e.g., phosphorus) were possibly involved (Cui et al., 2016; Xiao et al., 2016; Bowyer et al., 2017; Wood et al., 2017a, 2017b; Wood, 2018).

Among these environmental parameters, the changed Mg/Ca ratio in the oceans has been considered to chemically facilitate calcareous skeletization (Wood et al., 2017a, 2017b; Wood, 2018).

Previous studies have revealed that the seawater Mg/Ca ratio has fluctuated between ~1 and ~5 in the Phanerozoic, resulting in variations of bio-carbonate polymorphs between "aragonite seas" ( $Mg/Ca > 2$ ) and "calcite seas" ( $Mg/Ca < 2$ ) (Sandberg, 1983; Hardie, 1996; Stanley and Hardie, 1998; Lowenstein et al., 2001). However, the seawater Mg/Ca variation on the eve of the earliest macrobiota biomineralization is enigmatic, because reliable archives of seawater chemistry, such as animal skeletons, marine calcium carbonates, and evaporites, are rare in the Precambrian (Sandberg, 1983; Horita et al., 2002). Based on a mid-ocean ridge and river flux mixing model,

\* Corresponding authors.

E-mail addresses: [hkj@nwu.edu.cn](mailto:hkj@nwu.edu.cn) (K.-J. Huang), [maoluo@nigpas.ac.cn](mailto:maoluo@nigpas.ac.cn) (M. Luo).

Proterozoic oceans are proposed to oscillate between “aragonite seas” and “calcite seas” (Hardie, 2003). In this context, the seawater Mg/Ca ratio fluctuated between ~1 and ~4.5 during the Neoproterozoic and remained around 2 at the late Ediacaran (Hardie, 2003). Similarly, analyses on fluid inclusions in evaporites revealed a close while slightly higher seawater Mg/Ca ratio, ranging from 4 to 6 at the latest Ediacaran (Lowenstein et al., 2001; Horita et al., 2002; Brennan et al., 2004). These findings indicate moderate to high seawater Mg/Ca ratios throughout the Ediacaran and a probably slight decrease at the terminal Ediacaran. By contrast, a Neoproterozoic “aragonite-dolomite sea” with an extremely high seawater Mg/Ca ratio (>10) was proposed to explain the abundant early dolomitization and syn-sedimentary precipitation of the fibrous dolomite cements in Neoproterozoic oceans (Hood et al., 2011; Hood and Wallace, 2012, 2018). Furthermore, recent studies on late Ediacaran dolomite depositions in South China and Siberia indicate this extremely high seawater Mg/Ca ratio (>10) likely persisted to the late Ediacaran (Wood et al., 2017b; Hu et al., 2020; Wang et al., 2020; Zhao et al., 2021), and then dramatically decreased (from >10 to ~2) before the occurrence of the earliest calcified metazoans (Wood et al., 2017b; Hood and Wallace, 2018). These conflicting viewpoints call into question the range and trend of seawater Mg/Ca ratio in terminal Ediacaran oceans and its potential role in animal biomimetic innovation. Therefore, reliable proxies to provide additional constraints on seawater Mg/Ca variation during this critical period is required.

Seawater Mg/Ca variations can be potentially recorded by seawater Mg isotopic signatures (Higgins and Schrag, 2015), because processes that introduce and remove Mg from seawater are associated with considerable Mg isotope fractionation (Higgins and Schrag, 2015; Li et al., 2015, 2019b; Bialik et al., 2018; Huang et al., 2018). Reconstructing the ancient seawater Mg isotopic compositions largely depends on the record and preservation of reliable archives, among which dolomite is most promising for its large Mg sink and the resistance to post-depositional alterations (Li et al., 2015, 2019b; Hu et al., 2017, 2019; Bialik et al., 2018). In this context, dolostones from the lower part of the Dengying Formation (terminal Ediacaran), Yangtze Block, South China were investigated in this study to constrain the contemporaneous seawater chemistry at the dawn of animal biomimeticization, because the middle part of the Dengying Formation had witnessed the appearance of pioneering biomimetic macrobiota *Cloudina* and other skeletalized taxa (Hua et al., 2003; Cai et al., 2019). Systematic sedimentological and petrographic investigations were conducted to

reconstruct the environmental contexts of dolostones from the Dengying Formation before constraining the seawater chemistry by applying detailed geochemical analyses (trace elements and C-O-Mg isotopes) on these dolomites. Our results support the presence of the “aragonite-dolomite sea” in a relatively anoxic shallow marine setting and emphasize the increased silicate-dominated weathering flux at the basal Dengying Formation. The enhanced silicate weathering likely be in favor of the following skeletonization of early animals.

## 2. Geological setting and stratigraphy

The Ediacaran era is a critical time interval in which the breakup of the Rodinia and the subsequent assembly of the Gondwana both occurred (Li et al., 2013). The South China Block rifted from the supercontinent assembly and was situated near the equatorial latitude during the Ediacaran (Li et al., 2013). Thick successions that accumulated in shallow water, slope, and deep-water environments were distributed across the South China Block at a passive continental margin since then (Zhu et al., 2007; Ding et al., 2019).

The fossiliferous Dengying Formation (ca. 551.1–538.8 Ma) of the late Ediacaran is sandwiched between the underlying Doushantuo Formation and the overlying Kuanchuanpu Formation in the southern region of Shaanxi Province (Fig. 1B) (Zhu et al., 2007), and is dominated by mixed siliciclastic and carbonate rocks that accumulated in supratidal to outer ramp settings (Jiang et al., 2011; Cui et al., 2019). The Dengying Formation has been a research focus due to the well-preservation of the earliest biomimetic fossils within its middle part (the Gaojiashan Member, Cai et al., 2010). The Dengying Formation consists of three units, including the Algal Dolomite, Gaojiashan, and Beiwian Members in ascending order (Fig. 1B). Such lithostratigraphic framework has been applied throughout the upper Yangtze Platform, and the Algal Dolomite Member has been studied previously regarding its sedimentary, petrographic, and geochemical characteristics as well as paleoenvironmental implications (Fig. 1A) (Cui et al., 2019; Ding et al., 2019; Hu et al., 2020; Wang et al., 2020; Zhao et al., 2021). The Algal Dolomite Member, with a thickness of up to ~600 m, develops abundant botryoidal-shaped dolomites in its lower-middle part (Fig. 1B) (Zhang et al., 2014; Cui et al., 2019; Hu et al., 2020). The overlying Gaojiashan Member consists of silty limestones, sandstones, and conglomerates. The Beiwian Member is mainly composed of dolostones (Fig. 1B) (Cui et al., 2019). Besides, some studies suggest that there might be one more member composed of

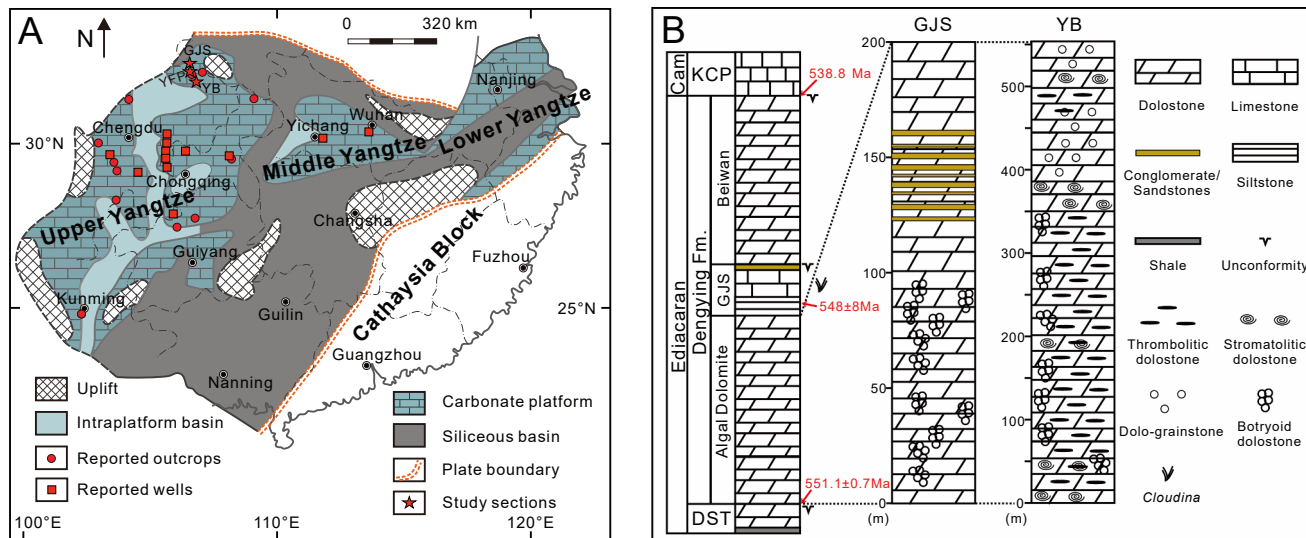


**Fig. 1.** (A) Paleogeographic map of the terminal Ediacaran Yangtze Block, modified from Ding et al. (2019). Reported sites are from Hu et al. (2020); Wang et al. (2020). (B) Stratigraphy of the study sites, modified from Cui et al. (2016, 2019); Hu et al. (2020). Age data are from Condon et al. (2005); Cui et al. (2016); Linnemann et al. (2019). Abbreviations: GJS = Gaojiashan section; YB = Yangba section; YFP = Yafangping section; DST = Doushantuo Formation; KCP = Kuanchuanpu Formation; Cam = Cambrian.

argillaceous rocks underlying the Algal Dolomite Member (Wang et al., 2020). The duration of the Algal Dolomite Member is constrained to  $\sim$  551–548 Ma according to the U-Pb zircon dating ( $551.1 \pm 0.7$  Ma) on the Doushantuo-Dengying boundary ash layer (Condon et al., 2005) and the detrital zircon age ( $548 \pm 8$  Ma) within the siltstone of the overlying Gaojiashan Member (Fig. 1B) (Cui et al., 2016). The studied sites here include the following three. One is the Gaojiashan (GJS) section located at Gaojiashan village, Ningqiang County, Hanzhong City of Shaanxi Province. The second is the Yangba (YB) section located at Yangba town, Nanjiang county, Bazhong City of Sichuan Province. The rest is the Yafangping (YFP) section which is located on the border region of the two provinces (Fig. 1A). Dolostone samples were collected from the lower part of the Algal Dolomite Member, with 16 from GJS, 64 from YB, and two from YFP.

### 3. Methods

Large hand samples, polished slabs, and corresponding thin sections were prepared for petrographic, cathodoluminescent, and geochemical investigations. Here, we applied *in situ* geochemical analyses to analyze the trace elements on thin sections, and conducted elemental and C-O-Mg isotopic measurements for texture-specific components. All experiments and lab work were undertaken at the State Key Laboratory of the Continental Dynamics (SKLCD), Department of Geology, Northwest University, China.

#### 3.1. Microscopy petrology

Microscopy and CL screening were conducted on dolomite thin sections to characterize the different sedimentary and diagenetic phases, and recognize the well-preserved marine primary carbonate phases. An International In-corporation (BII) CLF-1 cathodoluminescence device connected to a Nikon LV100N POL transmission microscope was used for the observation of both petrographic and CL features. The CL images were taken at a vacuum pressure under 0.003 mbar, and the power supply was 100–230 V (10 A). The output voltage/current was 40 kV/2 mA.

#### 3.2. Major and trace elements measurements

Based on detailed petrographic observations of thin sections, fabric-specific powder samples were drilled from polished slabs using a microscope-mounted drilling assembly. About 10 mg of drilled powder was weighed and dissolved in 4 mL 2% HNO<sub>3</sub>. Splits of solution were diluted in 2% HNO<sub>3</sub> for elemental analyses. Major (Ca and Mg) and trace elements (Na, K, Mn, and Sr) were measured using Thermo iCAP PRO ICP-OES. Gravimetrically prepared standard solutions were used to calibrate the concentration curve, and dolomite reference material JDO-1 was used for monitoring. The uncertainties for measured elements (Ca, Mg, Na, K, Mn, and Sr) were better than 10%.

Fabric-specific trace elements analyses based on *in situ* laser ablation inductively coupled plasma mass spectrometry (LA-ICP-MS) were conducted for selected thin sections to elaborately constrain the sedimentary contexts of the different dolomite components. Major and trace elements, including Al, Zr, Sc, Sr, Th, and rare earth elements and yttrium (REY) concentrations were determined by LA-ICP-MS on polished, 100  $\mu$ m thick thin sections. Laser sampling was conducted using Agilent 7900  $\times$  quadrupole ICP-MS equipped with a Helex 193 nm ArF excimer laser ablation system. Each analysis contains a background acquisition of approximately 20–30 s (gas blank) followed by 50 s data acquisition. Operating conditions include a laser frequency of 10 Hz and an ablation time of 60 s with a spot size of 120  $\mu$ m. The Agilent Chemstation was utilized for the acquisition of each analysis. Element contents were calibrated against multiple-reference materials (MACS-3, BCR-2G, BHVO-2G, NIST 610, and NIST 612), and calculated stoichiometric concentrations for dolomite were used as internal

standardization. Blocks of approximately 50 spot analyses on four different samples were analyzed at a time with standard materials analyzed every  $\sim$ 7 samples. The preferred values of element concentrations for the USGS reference materials are from the GeoReM database. Results were performed offline by ICPMS DataCal. Calcium was used as an internal standard, and integration of background and analyte signals, as well as time-drift correction, were calculated at the same time (Liu et al., 2008).

The obtained REY mass fractions were normalized to the Post Archean Australian Shale (PAAS) values (McLennan, 1989). The normalized values were used to calculate elemental anomalies through the following equations (Lawrence et al., 2006):

$$La/La^* = La_n / [Pr_n \times (Pr_n/Nd_n)^2] \quad (1)$$

$$Ce/Ce^* = Ce_n / [Pr_n \times (Pr_n/Nd_n)] \quad (2)$$

$$Eu/Eu^* = Eu_n / (Sm^2_n \times Tb_n)^{1/3} \quad (3)$$

In addition, (Nd/Yb)<sub>n</sub>, (Tb/Yb)<sub>n</sub>, and (Nd/Tb)<sub>n</sub> ratios were used to assess LREY/HREY, MREY/HREY, and LREY/MREY proportions respectively.

#### 3.3. Carbon and oxygen isotopes analyses

Carbonate carbon and oxygen isotopes were analyzed on a gas bench & isotope ratio mass spectrometry (delta-V advantage) at SKLCD. A refined method was used for the analyses and corrections of the  $\delta^{13}\text{C}$  and  $\delta^{18}\text{O}$  values. Up to 66 samples of each batch were loaded into 10 mL glass vials and sealed with septa, two standard samples were added every 6 sample-interval for monitoring and correction. All samples were flushed with 99.999% Helium for 5 min to eliminate the influence of natural air. Then the orthophosphoric acid was added at 70 °C for the release of CO<sub>2</sub> in samples. The carbon dioxide analyte gas was isolated via gas chromatography, and water was removed using a Nafion trap. The C and O isotope values are both reported in per mil relative to the international Vienna Pee Dee Belemnite (VPDB) standards with analytical precisions (SD) better than 0.15‰.

#### 3.4. Mg Isotope analyses

The purification of Mg was conducted in the ultra-clean lab of SKLCD. Herein we conducted a refined procedure for Mg purification, with the sample digestion, column chemistry, and isotopic analyses processes following the established procedures (Bao et al., 2019). Samples that contain 10–40  $\mu$ g Mg were digested in 1 N HCl and prepared for purification. Two columns filled with Bio-Rad AG50W-X12 resin (200–400 mesh) were used to separate Mg from Ca and other matrix metals respectively. Each column was processed twice for all samples and reference materials. The recovery of Mg for the column chemistry was  $>$  99%. The total blank of the complete procedure was  $<$ 25 ng Mg, which is negligible compared to the mass of Mg analyzed. The purified Mg solutions were dried down and then dissolved with 3% HNO<sub>3</sub> for isotopic measurement. Around 1 ppm sample was introduced by a 'wet' plasma system to analyze the Mg isotopic ratio using a Nu Plasma II MC-ICPMS (Wrexham, UK). The typical signal sensitivity for <sup>24</sup>Mg was about 8 V/ppm in the low-resolution mode. The instrumental fractionation was calibrated using a pure Mg solution GSB with the standard-sample-standard bracketing method (SSB), and the concentration and acidity between samples and standards were carefully matched. The measured Mg isotope ratios are reported in the delta notation ( $\delta$ ) as relative deviations to the DSM3 standard, and Mg isotope fractionation between phases A and B is expressed as their relative  $\delta$  value:

$$\delta^{\text{x}}\text{Mg} (\%) = \left\{ \frac{(\text{xMg}/\text{Mg})_{\text{sample}}}{(\text{xMg}/\text{Mg})_{\text{DSM3}}} - 1 \right\} \times 1000 \quad (4)$$

$$\Delta^{\text{x}}\text{Mg}_{\text{A-B}} = \delta^{\text{x}}\text{Mg}_{\text{A}} - \delta^{\text{x}}\text{Mg}_{\text{B}} \quad (5)$$

where  $\times$  refers to mass 25 or 26,  $\Delta^{\text{x}}\text{Mg}_{\text{A-B}}$  means  $\delta$  value difference of  $\text{xMg}$  between A and B. The long-term internal precision based on replicate runs of DSM3 and GSB is better than 0.06‰ for two times standard deviations (2SD) (Bao et al., 2019). The  $\delta^{26}\text{Mg}$  values for seawater and the USGS basalt standards (BCR-2 and BHVO-2) are  $-0.83 \pm 0.05\%$  (2SD,  $n = 3$ ),  $-0.23 \pm 0.06\%$  ( $n = 3$ ) and  $-0.26 \pm 0.06\%$  ( $n = 2$ ), respectively. These values are consistent with published data (Ling et al., 2011; Teng et al., 2015; Bao et al., 2019).

## 4. Results

### 4.1. Petrological features

The lower-middle part of the Algal Dolomite Member mainly consists of microbial dolomites (stromatolites and thrombolites) and botryoidal dolomites (Fig. 1B). Stromatolitic dolomites exhibit stratified columnar structures consisting of alternating dark and light laminated layers (Fig. 2A and 3A). These discernable laminations are composed of micritic dolomite (MM) and microcrystalline dolomite (MCD) (Fig. 3A). Thrombolites are characterized by clotted structures that consist of micro-clots and peloids (Fig. 2B and 3C). Both stromatolites and thrombolites show none-to-dull red colors under CL images (Fig. 3B and D). The rest porosity is filled by sparry crystalline dolomites (Fig. 2 and 3A–D).

On bedding planes, botryoidal dolomites are grape-shaped, grey to dark-grey, (hemi-) spheric aggregates that are mostly 0.5 to 5 cm in diameters (Fig. 2B). In vertical profile, these botryoidal dolomites either exhibit concentric layers around a core or form layered wavy to irregular

crusts that are parallel to bedding planes (Fig. 2C). Botryoidal dolomite mainly consists of matrix dolomites (micritic dolomite and micro-crystalline dolomites, MD), fibrous dolomite cements (FD), and sparry void-filling crystalline dolomite cements (CD) (Figs. 2–3).

FD usually grows perpendicularly from the microbialite dolomites or occludes the voids of microbialite frameworks as early-generation cements, and occasionally transits from isopachous fibrous dolomite crust which directly lies on the dolomite matrix (Fig. 2B–D). The concentric, isopachous FD grows perpendicularly from the core of individual botryoidal dolomites (Fig. 2C–D). FD shows laterally continuous growth bands, with alternating light and dark zones which are defined by various inclusion densities under polarized light, and displaying non to dull red/purple rhythmic luminescence zones under CL (Fig. 3E–F). These cements are constituted by isopachous sub-crystals that are usually  $<100 \mu\text{m}$  in width while up to  $\sim 3 \text{ mm}$  in length (Fig. 3E–H). These sub-crystals have characteristic features (Fig. 3E–H). One common type is fan-like, fibrous sub-crystals forming bundles (Fig. 3G). It exhibits undulose extinction in a reverse direction relative to the rotation of the rotary stage (Fig. 3G). Another type is blade-shaped, fibrous crystals that show unit extinction (Fig. 3H). Both types of cements display length-slow optical characteristics. These two types of cements can be categorized as fascicular slow dolomite cements (FSD) and radial slow dolomite cements (RSD) respectively based on their morphology and extinction characteristics. The two types of cements have been defined as primary dolomite precipitates in Neoproterozoic oceans from previous studies (Hood et al., 2011; Hood and Wallace, 2012, 2018).

CD usually fills the rest space of the void as the late-stage cements. They consist of medium- to coarse-grained crystals and are characterized by mottled, dull-bright red luminescence under CL (Figs. 2D and 3 A–F).

### 4.2. REY concentrations and distribution patterns

All samples show low  $\sum\text{REY}$  concentrations, ranging from 0.22 to

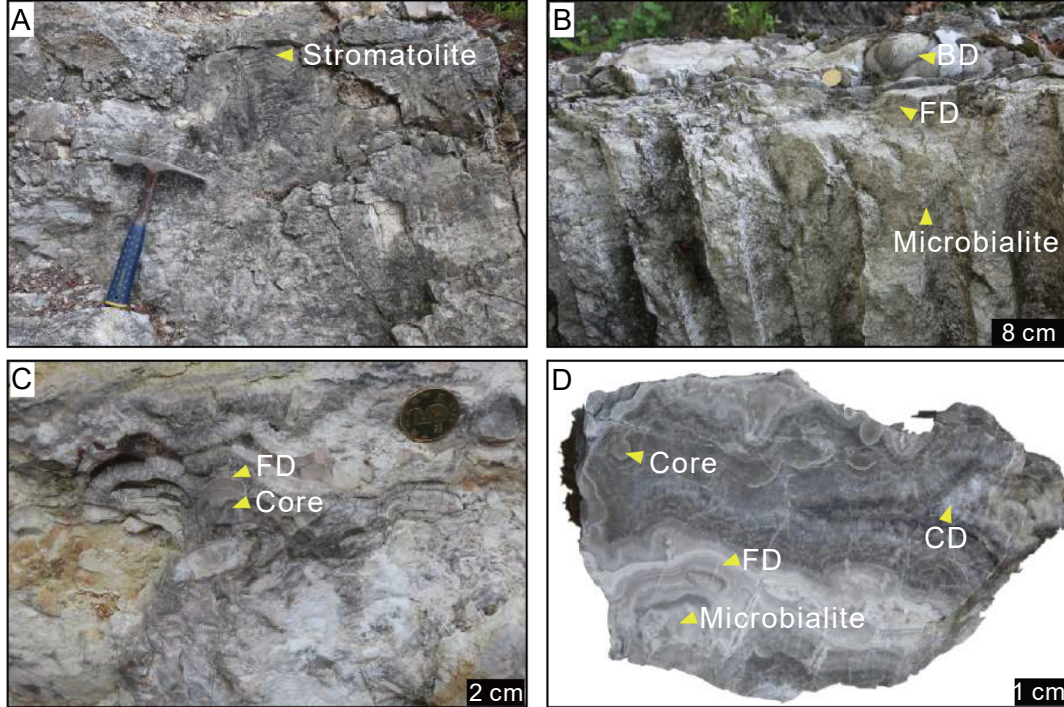


**Fig. 2.** Representative field and hand specimen photographs of the sedimentary structure of botryoidal dolomite. (A) Microbialite sedimentary beddings in the Algal Dolomite Member of the GJS section. (B) The morphology of botryoidal dolostone and the sedimentary relationship between botryoidal dolostone and hosting dolostones from the YB section. (C) The vertical profile of botryoidal dolostone and the sedimentary relationship between botryoidal dolostone and hosting rocks from the GJS section. (D) A polished slab shows microbialites, fibrous dolomite cements, and void-filling crystalline dolomite cements. BD, FD, and CD are abbreviations for botryoidal dolostones, fibrous dolomite cements, and crystalline dolomite cements.

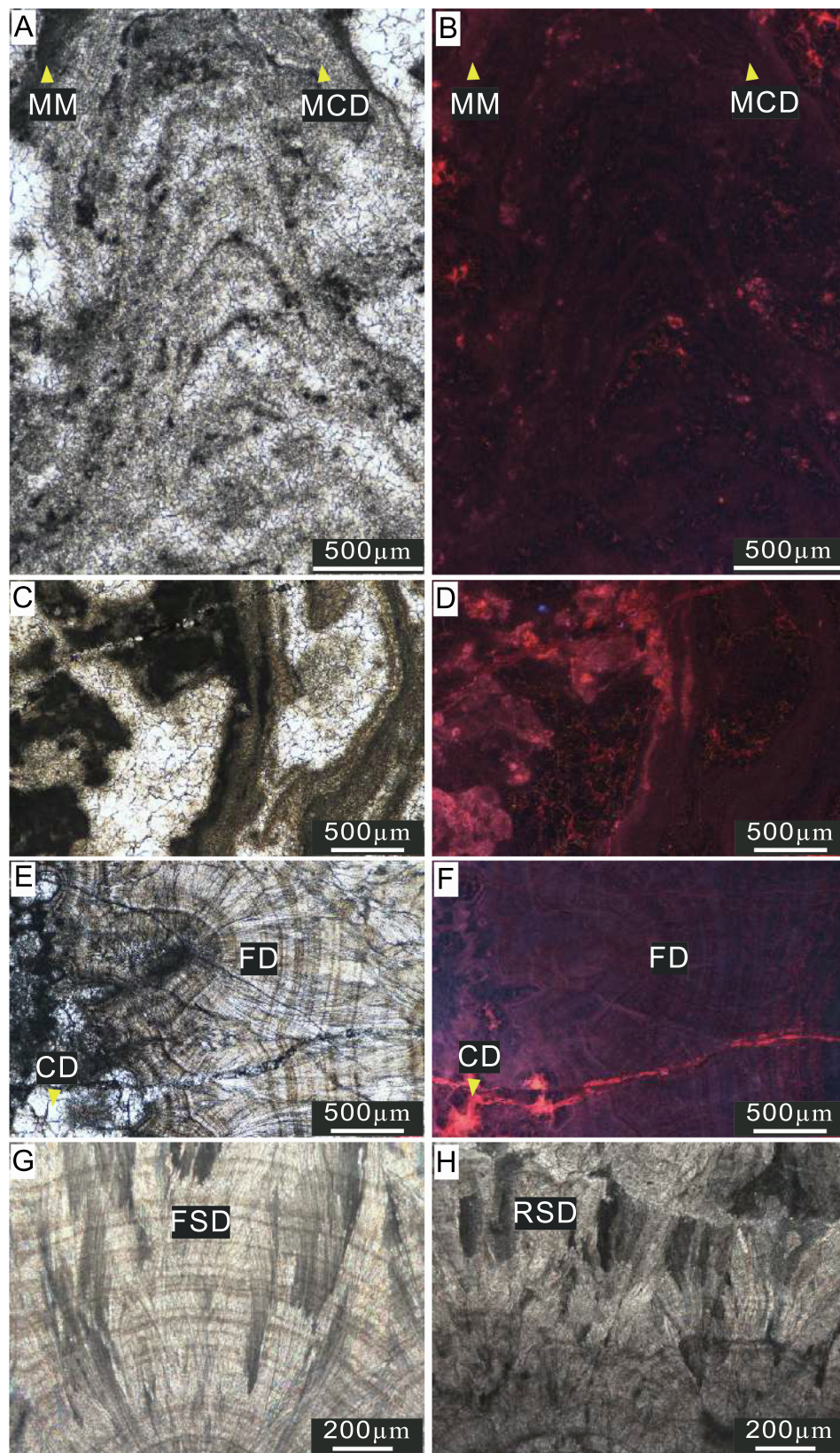


**Fig. 3.** Petrological and cathodoluminescent features under microscopy. (A–B) Domal-shaped stromatolites showing alternating micritic dolomites dark laminae and micro-crystalline bright laminae, in polarized light and cathodoluminescent photomicrograph respectively. (C–D) Thrombolites which dominantly consist of micritic dolomite show clotted microbial textures, in polarized light cathodoluminescent photomicrograph respectively. (E–F) Fibrous dolomite cements, growing from micritic and/or micro-crystalline microbialite dolomite matrix, and the rest pores are cemented by the late-stage coarse crystalline dolomites, in polarized light and cathodoluminescent photomicrograph respectively. (G) Fan-like, fibrous crystals form bundles within isopachous cements, displaying undulose extinction in a reverse direction relative to the rotation direction when rotating the microscope stage. (H) Blade-shaped fibrous dolomite crystals that show unit extinction.

4.92 ppm, and mostly between 0.50 and 2.00 ppm with an average value of 1.42 ppm (Table 1; Fig. 4A). Terrigenous sourced elements, such as Al, Zr, Sc, and Th, show low concentrations, and the data have been screened with the criteria of  $\text{Al} < 200 \text{ ppm}$ ,  $\text{Ba/Nd} < 100$ , and  $\text{Y/Ho} > 33$  to further exclude contaminations of detrital materials on REY

concentrations and the influence of Ba on Nd (Table 1). The Ce anomaly spans a wide range from 0.22 to 1.97, with the majority values within  $1.0 \pm 0.3 \text{ ppm}$  (Table 1). The Y/Ho ratios range from 34.6 to 330 with most values between 50 and 100 and an average value of 71 (Table 1). The La anomaly ranges from 0.37 to 5.12 with an average value of 1.7

**Table 1**

The concentrations (ppm) of Al, Sc, Zr, Th and REY concentrations, and elemental ratios of various components including microbialite dolomites (MD), fibrous dolomite cements (FD), and late-stage void-filling crystalline dolomite cements (CD).

Sample	Height (m)	Type	Al	Sc	Zr	Th	La	Ce	Pr	Nd	Sm	Eu	Gd	Tb	Dy	Y	Ho	Er	Tm	Yb	Lu	$\sum$ REY	Ce/ Ce*	La/ La*	Y/Ho	(Nd/ Yb) <sub>n</sub>	(Dy/ Sm) <sub>n</sub>	(La/ Sm) <sub>n</sub>
G5-4	7.1	MD	48	0.01	0.41	0.01	0.109	0.182	0.015	0.073	0.015	0.003	0.010	0.002	0.007	0.095	0.001	0.002	0.000	0.002	0.001	0.52	1.68	2.62	71.1	3.78	0.55	1.05
G14-2	33.4	MD	101	0.05	0.60	0.01	0.097	0.135	0.017	0.053	0.019	0.002	0.013	0.000	0.016	0.093	0.001	0.007	0.000	0.009	0.001	0.46	0.75	0.94	62.7	0.51	1.03	0.75
G14-24	33.4	MD	107	0.02	1.84	0.02	0.103	0.202	0.022	0.085	0.014	0.005	0.024	0.003	0.019	0.190	0.004	0.011	0.001	0.005	0.000	0.69	1.03	1.11	43.8	1.39	1.63	1.08
G1-22	41.4	FD	101	0.04	1.50	0.11	0.499	0.946	0.112	0.498	0.077	0.020	0.080	0.009	0.054	0.494	0.011	0.020	0.001	0.008	0.000	2.83	1.09	1.39	45.8	4.93	0.84	0.95
G1-25	41.4	FD	109	0.01	0.00	0.00	0.089	0.396	0.062	0.254	0.069	0.005	0.051	0.006	0.045	0.370	0.007	0.030	0.001	0.013	0.001	1.40	0.75	0.37	51.3	1.65	0.78	0.19
G13-16	32.4	FD	78	0.03	0.18	0.00	0.060	0.081	0.012	0.056	0.002	0.001	0.002	0.001	0.008	0.085	0.002	0.003	0.001	0.007	0.002	0.32	0.86	1.59	37.6	0.66	3.77	3.64
G14-7	33.4	FD	65	0.05	0.00	0.00	0.116	0.355	0.044	0.189	0.037	0.010	0.038	0.005	0.019	0.231	0.004	0.019	0.001	0.006	0.002	1.07	1.01	0.77	55.5	2.68	0.59	0.45
G2-12	39.4	CD	65	0.02	0.13	0.00	0.072	0.148	0.015	0.062	0.005	0.001	0.007	0.002	0.008	0.076	0.001	0.006	0.000	0.004	0.000	0.41	1.13	1.20	98.3	1.39	1.89	2.09
G6-15	9.7	CD	73	0.00	0.00	0.00	0.074	0.335	0.056	0.242	0.073	0.018	0.059	0.012	0.020	0.372	0.007	0.017	0.001	0.011	0.001	1.30	0.76	0.39	56.8	1.75	0.32	0.15
G8-9	15.7	CD	63	0.02	0.02	0.00	0.482	1.683	0.230	0.985	0.192	0.044	0.127	0.023	0.100	0.970	0.020	0.040	0.003	0.020	0.002	4.92	0.91	0.60	49.19	4.10	0.62	0.37
Y22-1	33.0	MD	31	0.03	0.64	0.00	0.221	0.289	0.022	0.110	0.016	0.006	0.009	0.002	0.004	0.138	0.003	0.016	0.000	0.007	0.001	0.84	1.97	4.14	101.3	1.25	0.32	2.00
Y22-11	33.0	MD	113	0.00	1.43	0.00	0.193	0.252	0.024	0.135	0.020	0.008	0.012	0.002	0.021	0.120	0.002	0.003	0.001	0.012	0.002	0.81	1.76	4.17	120.5	0.91	1.30	1.43
Y26-3	35.5	MD	78	0.02	0.70	0.03	0.281	0.433	0.044	0.171	0.015	0.011	0.012	0.002	0.030	0.229	0.003	0.020	0.001	0.005	0.001	1.26	1.10	1.51	101.8	3.05	2.35	2.70
Y36-6	45.5	MD	89	0.04	0.68	0.03	0.414	0.565	0.057	0.242	0.047	0.010	0.038	0.004	0.028	0.298	0.005	0.011	0.001	0.018	0.002	1.74	1.23	2.09	61.7	1.13	0.72	1.29
Y36-13	45.5	MD	95	0.01	0.84	0.03	0.070	0.203	0.016	0.037	0.016	0.001	0.002	0.000	0.009	0.089	0.001	0.012	0.000	0.008	0.002	0.47	0.90	0.40	68.3	0.37	0.64	0.64
Y44-7	57.2	MD	105	0.00	3.29	0.00	0.525	0.796	0.085	0.436	0.062	0.025	0.045	0.010	0.050	0.542	0.009	0.036	0.003	0.037	0.001	2.66	1.40	2.59	57.6	0.98	0.97	1.24
Y44-8	57.2	MD	38	0.02	0.25	0.00	0.348	0.511	0.065	0.245	0.050	0.011	0.048	0.008	0.029	0.330	0.010	0.023	0.002	0.007	0.001	1.69	0.87	1.22	117.5	2.92	0.69	1.01
Y44-9	57.2	MD	174	0.01	0.51	0.04	0.312	0.461	0.051	0.165	0.061	0.006	0.022	0.003	0.019	0.230	0.005	0.020	0.001	0.009	0.001	1.36	0.84	0.99	44.8	1.49	0.37	0.74
Y44-10	57.2	MD	73	0.00	0.35	0.03	0.288	0.423	0.043	0.171	0.026	0.006	0.028	0.007	0.024	0.212	0.004	0.018	0.000	0.014	0.002	1.27	1.12	1.65	76.9	1.02	1.06	1.58
Y44-12	57.2	MD	134	0.03	0.52	0.03	0.191	0.285	0.031	0.154	0.027	0.006	0.049	0.003	0.018	0.163	0.002	0.006	0.001	0.007	0.001	0.94	1.32	2.37	78.2	1.83	0.79	1.04
Y44-15	57.2	MD	114	0.00	0.57	0.02	0.346	0.450	0.053	0.178	0.041	0.006	0.028	0.004	0.022	0.243	0.002	0.014	0.001	0.005	0.002	1.40	0.83	1.16	55.3	3.22	0.63	1.23
Y45-9	61.2	MD	87	0.04	0.90	0.00	0.431	0.213	0.072	0.283	0.046	0.013	0.059	0.008	0.042	0.701	0.007	0.026	0.004	0.023	0.002	1.93	0.93	1.43	84.6	1.01	1.09	1.37
Y46-11	65.2	MD	153	0.06	0.72	0.02	0.303	0.328	0.047	0.155	0.030	0.007	0.019	0.003	0.020	0.250	0.002	0.005	0.002	0.005	0.002	1.18	0.66	1.08	123.8	2.57	0.81	1.48
Y46-15	65.2	MD	161	0.04	0.26	0.01	0.596	0.573	0.080	0.285	0.023	0.008	0.050	0.007	0.039	0.544	0.008	0.021	0.002	0.018	0.003	2.26	0.74	1.48	63.5	1.30	2.05	3.81
Y46-16	65.2	MD	111	0.00	0.18	0.01	0.319	0.359	0.054	0.172	0.024	0.007	0.035	0.002	0.027	0.317	0.005	0.012	0.002	0.013	0.001	1.35	0.62	0.96	34.6	1.09	1.30	1.89
Y46-17	65.2	MD	149	0.00	0.53	0.01	0.324	0.333	0.047	0.168	0.024	0.009	0.033	0.003	0.029	0.303	0.004	0.011	0.001	0.013	0.002	1.31	0.74	1.41	48.7	1.07	1.43	1.93
Y46-20	65.2	MD	52	0.03	0.54	0.03	0.395	0.493	0.065	0.183	0.033	0.009	0.049	0.006	0.026	0.416	0.008	0.022	0.002	0.008	0.001	1.72	0.63	0.77	63.3	1.90	0.95	1.76
Y46-28	65.2	MD	129	0.03	0.84	0.06	0.743	1.422	0.118	0.439	0.083	0.023	0.074	0.014	0.076	0.863	0.018	0.038	0.003	0.035	0.004	3.95	1.30	1.37	68.3	1.03	1.08	1.30
Y56-1	91.7	MD	82	0.03	0.67	0.03	0.021	0.029	0.005	0.022	0.002	0.004	0.002	0.003	0.002	0.043	0.001	0.003	0.001	0.002	0.000	0.14	0.66	1.06	49.4	1.05	0.75	1.25
Y56-6	91.7	MD	96	0.05	0.64	0.03	0.118	0.149	0.018	0.085	0.013	0.003	0.013	0.000	0.017	0.205	0.002	0.002	0.003	0.000	0.063	1.11	2.24	46.7	2.13	1.51	1.28	
Y56-7	91.7	MD	28	0.03	0.13	0.00	0.289	0.432	0.058	0.240	0.032	0.016	0.040	0.006	0.039	0.468	0.006	0.023	0.001	0.011	0.004	1.66	0.90	1.36	66.0	1.81	1.46	1.32
Y56-13	91.7	MD	45	0.01	0.90	0.01	0.119	0.179	0.023	0.091	0.013	0.005	0.016	0.002	0.014	0.246	0.004	0.007	0.001	0.011	0.001	0.73	0.89	1.27	74.8	0.67	1.26	1.33
Y67-1	143.8	MD	177	0.03	0.48	0.00	0.236	0.339	0.037	0.131	0.023	0.006	0.025	0.003	0.039	0.760	0.008	0.022	0.004	0.028	0.003	1.66	0.93	1.24	92.3	0.39	2.03	1.51
Y26-5	35.5	FD	121	0.03	0.67	0.01	0.226	0.352	0.042	0.149	0.021	0.010	0.023	0.004	0.021	0.160	0.004	0.010	0.001	0.011	0.001	1.04	0.84	1.02	37.7	1.09	1.23	1.60
Y28-4	38.0	FD	82	0.01	0.76	0.00	0.168	0.330	0.046	0.195	0.048	0.011	0.032	0.006	0.022	0.253	0.006	0.017	0.003	0.005	0.001	1.14	0.88	1.03	39.8	3.46	0.54	0.50
Y28-6	38.0	FD	91	0.00	0.42	0.00	0.439	0.439	0.076	0.362	0.055	0.019	0.097	0.006	0.044	0.534	0.013	0.028	0.002	0.014	0.001	2.42	1.34	2.08	41.7	2.12	0.96	1.16
Y34-4	42.5	FD	33	0.04	0.34	0.01	0.172	0.362	0.038	0.167	0.016	0.008	0.009	0.006	0.021	0.190	0.005	0.016	0.001	0.010	0.003	1.02	1.21	1.37	36.8	1.42	1.56	1.58
Y34-5	42.5	FD	100	0.04	0.25	0.01	0.399	0.753	0.090	0.290	0.050	0.010	0.054	0.007	0.047	0.427	0.010	0.030	0.001	0.019	0.005	2.19	0.78	0.73	42.0	1.26	1.12	1.16
Y36-1																												

Table 1 (continued)

Sample	Height (m)	Type	Al	Sc	Zr	Th	La	Ce	Pr	Nd	Sm	Eu	Gd	Tb	Dy	Y	Ho	Er	Tm	Yb	Lu	$\sum$ REY	Ce/ $\text{Ce}^*$	La/ $\text{La}^*$	Y/Ho	Nd/Yb <sub>n</sub>	Dy/Yb <sub>n</sub>	La/Sm <sub>n</sub>
Y52-5	85.2	FD	132	0.03	0.99	0.09	0.367	0.573	0.061	0.264	0.042	0.008	0.048	0.005	0.023	0.269	0.006	0.007	0.003	0.011	0.001	1.69	1.18	1.77	44.5	2.02	0.66	1.27
Y56-5	91.7	FD	23	0.00	0.32	0.00	0.075	0.083	0.007	0.031	0.004	0.002	0.004	0.001	0.008	0.096	0.001	0.002	0.001	0.003	0.001	0.32	1.56	3.43	145.3	0.83	2.26	2.56
Y59-22	99.7	FD	27	0.02	0.46	0.00	0.165	0.164	0.024	0.093	0.006	0.003	0.014	0.002	0.012	0.364	0.004	0.020	0.001	0.006	0.001	0.88	0.76	1.60	90.5	1.22	2.30	3.73
Y59-25	99.7	FD	20	0.02	1.35	0.00	0.089	0.044	0.008	0.041	0.009	0.003	0.006	0.002	0.013	0.239	0.001	0.015	0.002	0.007	0.001	0.48	0.86	4.95	330.1	0.52	1.70	1.45
Y59-27	99.7	FD	12	0.02	2.86	0.00	0.088	0.063	0.012	0.070	0.005	0.002	0.002	0.001	0.004	0.265	0.003	0.006	0.000	0.003	0.001	0.53	0.82	3.55	83.5	1.74	1.14	2.82
Y59-28	99.7	FD	20	0.01	1.31	0.00	0.072	0.053	0.007	0.041	0.009	0.003	0.010	0.001	0.006	0.203	0.003	0.015	0.001	0.015	0.002	0.44	1.22	5.12	65.7	0.23	0.76	1.19
Y59-31	99.7	FD	32	0.03	0.24	0.00	0.241	0.273	0.030	0.149	0.017	0.006	0.016	0.003	0.038	0.405	0.002	0.022	0.001	0.011	0.002	1.22	1.22	3.00	243.2	1.12	2.65	2.05
Y60-4	109.7	FD	26	0.02	0.48	0.00	0.117	0.161	0.017	0.068	0.011	0.004	0.021	0.002	0.010	0.149	0.003	0.003	0.000	0.002	0.001	0.57	1.07	1.68	48.4	3.48	1.06	1.55
Y67-3	143.2	FD	37	0.02	0.80	0.00	0.098	0.113	0.011	0.057	0.008	0.004	0.016	0.002	0.005	0.378	0.004	0.014	0.002	0.003	0.002	0.72	1.54	3.76	84.7	1.59	0.75	1.72
Y67-4	143.2	FD	25	0.00	1.48	0.00	0.099	0.107	0.011	0.066	0.009	0.005	0.014	0.001	0.011	0.254	0.002	0.009	0.001	0.005	0.000	0.59	1.57	4.57	110.6	1.17	1.49	1.69
Y83-4	226.2	FD	22	0.02	1.10	0.01	0.064	0.102	0.015	0.051	0.006	0.002	0.006	0.001	0.009	0.070	0.001	0.002	0.001	0.002	0.001	0.33	0.70	0.84	55.1	2.79	1.76	1.49
Y83-6	226.2	FD	170	0.05	0.76	0.05	0.197	0.271	0.029	0.117	0.028	0.001	0.013	0.003	0.013	0.204	0.003	0.013	0.000	0.003	0.001	1.07	1.70	1.70	73.3	3.32	0.54	1.02
Y28-2	38.0	CD	168	0.03	0.05	0.00	0.414	1.453	0.100	0.375	0.063	0.034	0.038	0.004	0.065	0.501	0.013	0.028	0.001	0.018	0.001	3.11	1.58	0.91	39.4	1.75	1.23	0.96
Y28-3	38.0	CD	100	0.00	0.62	0.01	0.278	0.938	0.148	0.627	0.178	0.034	0.122	0.019	0.096	0.682	0.019	0.039	0.003	0.022	0.002	3.21	0.78	0.53	36.0	2.35	0.64	0.23
Y28-5	38.0	CD	76	0.00	0.22	0.00	0.156	0.351	0.049	0.163	0.016	0.010	0.034	0.008	0.032	0.254	0.006	0.011	0.002	0.007	0.001	1.10	0.69	0.55	41.1	1.82	2.33	1.40
Y44-4	57.2	CD	143	0.01	1.10	0.00	0.356	0.632	0.070	0.305	0.059	0.013	0.041	0.006	0.037	0.334	0.005	0.016	0.001	0.019	0.002	1.90	1.15	1.54	60.9	1.31	0.74	0.88
Y45-8	61.2	CD	57	0.03	0.40	0.01	0.145	0.329	0.036	0.141	0.022	0.002	0.012	0.001	0.020	0.169	0.003	0.000	0.001	0.007	0.001	0.89	1.06	1.00	75.9	1.65	1.11	0.98
Y52-1	85.2	CD	131	0.00	0.01	0.00	0.245	0.484	0.057	0.213	0.020	0.012	0.033	0.001	0.019	0.294	0.004	0.011	0.001	0.006	0.000	1.40	0.90	0.92	55.5	3.18	1.11	1.74
Y56-8	91.7	CD	22	0.02	1.43	0.00	0.126	0.465	0.071	0.311	0.063	0.035	0.067	0.008	0.047	0.480	0.009	0.025	0.002	0.015	0.004	1.73	0.84	0.54	48.8	1.73	0.88	0.29
Y74-10	164.7	CD	74	0.00	0.30	0.00	0.078	0.156	0.019	0.101	0.010	0.008	0.025	0.002	0.016	0.188	0.004	0.003	0.001	0.005	0.001	0.62	1.22	1.73	65.1	1.84	1.80	1.09

(Table 1). All dolomite components from the GJS and YB sections show flat to middle REY enriched (bell-shaped) distribution patterns (Fig. 5).

FD and MD components from both sections share similar REY concentrations and distribution patterns overall (Table 1). The  $\sum\text{REY}$  of MD, FD, and CD ranges from 0.46 to 0.69 ppm, 0.32 to 2.83 ppm, and 0.41 to 4.92 ppm respectively and with average values of 0.56, 1.41, and 2.21 ppm in the GJS section (Table 1). The  $\sum\text{REY}$  of MD, FD, and CD range from 0.14 to 3.95 ppm, 0.22 to 4.72 ppm, and 0.40 to 3.21 ppm respectively with average values of 1.43, 1.35, and 1.68 ppm in the YB section (Table 1). For the Ce anomaly, MD from GJS has slightly higher values (0.75 to 1.68, 1.15 on average) than those for FD (0.75 to 1.09, averagely 0.93) and CD (0.76 to 1.13 averagely 0.93), while CD (0.69 to 1.66, averagely 1.10) from the YB section has mildly higher values than that of MD (0.33 to 1.97, averagely 0.99) and FD (0.12 to 1.57, 0.99 on average) (Table 1; Fig. 4). The three components from the GJS section have similar Eu anomalies (1.03 to 1.48, averagely 1.21 for MD; 0.47 to 2.18, averagely 1.36 for FD; 0.95 to 1.24, averagely 1.21 for CD), and the larger dataset from the YB section indicates CD has a higher average Eu anomaly of 2.52 (1.08 to 4.59) than that of 1.70 and 1.80 for MD (0.66 to 4.12) and FD (0.24 to 4.09) (Table 1; Fig. 4).

#### 4.3. C and O isotopic compositions

The three components (MD, FD, and CD) have similar  $\delta^{13}\text{C}$  ranges within the same section. The  $\delta^{13}\text{C}$  values of these components from the GJS section are relatively uniform, with MD ranging from 1.14‰ to 3.10‰ (except for one higher value of 5.14‰) and averagely 2.11‰, FD ranging from 1.13‰ to 2.71‰ and has an average value of 1.92‰, and CD ranges from 1.41‰ to 2.30‰ and averagely 1.81‰ (Table 2; Fig. 6). While  $\delta^{13}\text{C}$  of samples from the YB section show higher values, which started from ~6‰ at the lower part and decreased to ~3‰ at ~100 m and maintained this value upward (Table 2; Fig. 6). The  $\delta^{13}\text{C}$  from YB also shows a slightly decreasing trend for MD (1.21‰ to 6.40‰, averagely 3.97‰), FD (1.65‰ to 5.62‰, averagely 3.43‰), and CD (1.93‰ to 4.52‰, averagely 3.05‰). Samples from the YFP section display similar  $\delta^{13}\text{C}$  values to the other two sections, with average values of 3.2‰ (2.69‰ to 3.70‰) and 3.46‰ (2.81‰ to 4.08‰) for MD and FD (Table 2; Fig. 6).

By contrast, CD samples have more negative  $\delta^{18}\text{O}$  values than that of MD and FD (averagely 2‰ lower at the GJS site and 4‰ lower at the YB site, Fig. 6). MD and FD from the YFP section have identical average  $\delta^{18}\text{O}$  values of -3.32‰ and -3.33‰, and similar ranges of -4.48‰ to -2.17‰ and -4.62‰ to -1.97‰ (Table 2). Similarly, samples from the GJS section show close  $\delta^{18}\text{O}$  values for MD and FD (-3.36‰ and -3.65‰ on average, and ranges from -7.64‰ to 0.36‰ and -6.20‰ to -0.79‰ respectively), while obviously lighter O isotopes for CD (between -11.48‰ and -1.47‰ with an average value of -5.48‰) (Table 2). Samples from the YB section display similar trends regarding their  $\delta^{18}\text{O}$  compositions, with average  $\delta^{18}\text{O}$  values of -3.19‰ (from -6.26‰ to -0.03‰), -3.78‰ (from -7.91‰ to -1.28‰), and -7.27‰ (from -11.25‰ to -0.92‰) for MD, FD, and CD respectively (Table 2). The  $\delta^{18}\text{O}$  values of most samples are above -10‰, except for three CD samples (one from the GJS and two from the YB respectively, Table 2; Fig. 6).

#### 4.4. Elemental and Mg isotopic compositions

The dolomite samples have Mg/Ca ratios between 1.01 and 1.06, which falls in the range of stoichiometric dolomite [Ca<sub>1.00–0.96</sub>Mg<sub>1.00–1.04</sub>(CO<sub>3</sub>)<sub>2</sub>] (Table 2; Fig. 7C). The  $\delta^{26}\text{Mg}$  values of all samples range from -1.64‰ to -2.25‰ (N = 36) with an average value of  $-2.01 \pm 0.28$ ‰ (2SD), and show no obvious stratigraphic trends for both the GJS and YB sections (Table 2; Figs. 6–7). The  $\delta^{26}\text{Mg}$  values of MD and FD show identical ranges and average values (MD ranges from -2.17‰ to -1.67‰ with an average value of -2.03‰, and FD ranges from -2.25‰ to -1.64‰ with an average value of -2.03‰), while that

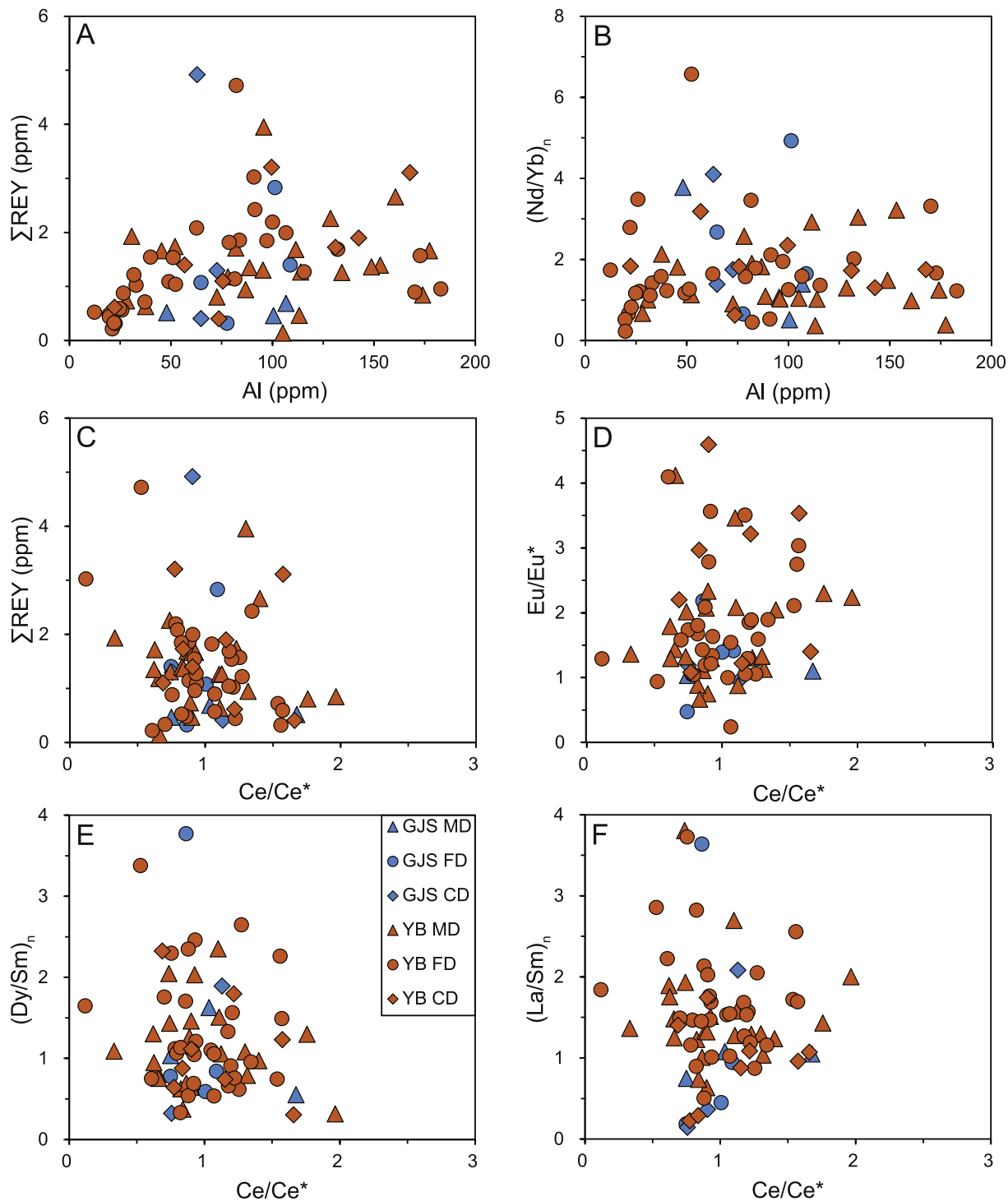


**Fig. 4.** Cross-plots of Al against  $\sum \text{REY}$  and  $(\text{Nd}/\text{Yb})_n$  ratio, Ce/ $\text{Ce}^*$  against Eu/ $\text{Eu}^*$ ,  $(\text{Dy}/\text{Sm})_n$ ,  $\sum \text{REY}$  and  $(\text{La}/\text{Sm})_n$  ratios for MD, FD and CD from the GJS and YB sections.

for CD is slightly heavier (ranges from  $-2.02\text{\textperthousand}$  to  $-1.77\text{\textperthousand}$ , averagely  $-1.93\text{\textperthousand}$ , Table 2; Fig. 7). The  $\delta^{26}\text{Mg}$  values are roughly correlated to Mn/Sr ratios and  $\delta^{18}\text{O}$  values for all samples as a whole (Fig. 7). The Na/(Mg + Ca) ratios range from 0.2 to 2.4 mmol/mol, and roughly correlate to  $\delta^{13}\text{C}$ ,  $\delta^{18}\text{O}$ , and  $\delta^{26}\text{Mg}$  values on the whole (Figs. 7–8). The K/(Mg + Ca) ratios range from 0.08 to 0.32 mmol/mol, and also roughly correlate to  $\delta^{26}\text{Mg}$  and  $\delta^{18}\text{O}$  values on the whole while with weaker trends (Fig. 8). The Na/(Mg + Ca) and K/(Mg + Ca) ratios are positively correlated, and Sr/(Mg + Ca) and  $\delta^{13}\text{C}$  are also correlated to  $\delta^{26}\text{Mg}$  values as a whole (Figs. 7–8).

## 5. Discussion

In this section, we firstly discuss the origin of dolomites in the Algal Dolomite Member of the Dengying Formation. Then we evaluate the potential of different dolomite components in recording the coeval seawater chemistry. The Mg isotopic variations are further applied to constrain the coeval seawater chemistry. Finally, we explore the possible role of seawater chemistry in favoring the early animal biomineralization during the terminal Ediacaran.

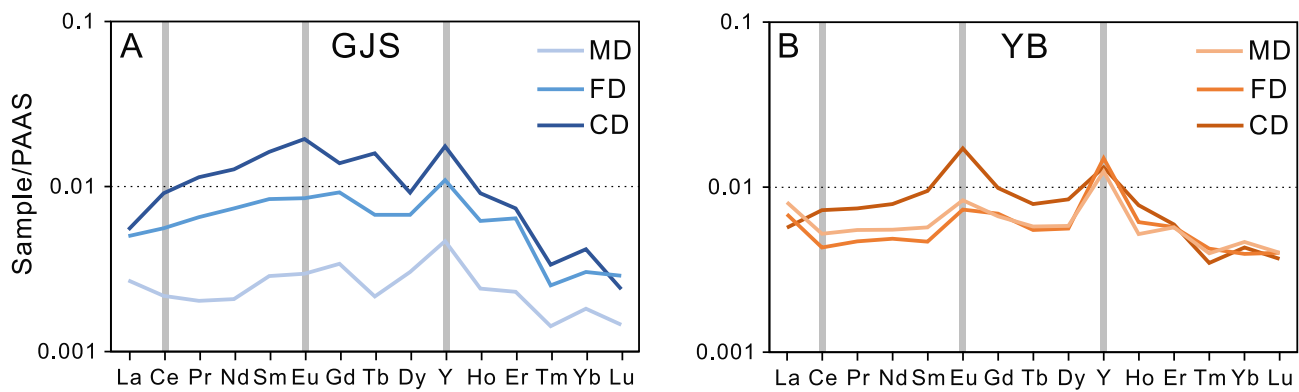


Fig. 5. The average normalized REY patterns of MD, FD and CD samples from the GJS and YB sections respectively.

### 5.1. Early dolomitization and syn-sedimentary dolomite cement precipitation

The widespread dolomitization in the Precambrian has substantially impeded the reconstruction of seawater chemistry through geochemical investigations of primary calcium carbonates. Thus, detailed petrographic identifications and geochemical investigations are required before applying Precambrian dolomite components to recover the past seawater chemistry (Hood and Wallace, 2012, 2014, 2018).

As the major components in MD, stromatolitic and thrombolitic dolomites are widely distributed within the lower-middle part of the Algal Dolomite Member. They have well-preserved fabrics that show non- to dull-luminescent CL characteristics (Fig. 3A–D). Such features suggest early dolomitization of metastable precursors (probably aragonite or high-Mg calcite) (Banerjee et al., 2019; Ding et al., 2019; Wang et al., 2020). The presence of these primary minerals is also supported by their depositional textures, such as the bladed cements, concentric cortices, and square/spiculate crystal terminations (Hood and Wallace, 2018; Cui et al., 2019; Hu et al., 2020; Zhao et al., 2021). The precipitation of the initial aragonite/high-Mg calcite was likely favored by the seawater chemistry and captured by microbials to form microbial fabrics (Lian et al., 2017; Hu et al., 2020), and then transformed to dolomite via mimetic dolomitization during syn-depositional diagenesis.

In addition to microbialites, multiple lines of evidence demonstrate that FD was likely primary cements that precipitated during the syn-sedimentary stage. Firstly, FD within botryoidal dolomites grows upon either microbialites or the botryoidal dolomite core, or fills the voids of the framework as first-generation cements (Figs. 2 and 3E–H), suggesting a syn-sedimentary origin (Lian et al., 2017). Furthermore, typical growth zonation and rhythmic luminescent characteristics of FD indicate the preservation of primary sedimentary structures (Fig. 3E–H), because the dolomitization of the precursor minerals would destroy these initial isopachous growth zones and CL features (Hood and Wallace, 2012). Most importantly, the well-preserved FSD and RSD that are widely developed in the Algal Dolomite Member have been suggested to represent primary dolomite cements in Neoproterozoic dolomite deposits (Hood et al., 2011; Hood and Wallace, 2012, 2018; Wang et al., 2020). These cements have length-slow characteristics, which are different from Phanerozoic length-fast aragonite and calcite minerals (Hood and Wallace, 2018). The dolomitization of calcite (trigonal, the same syngony as dolomite) would be syntaxial and its length-fast crystallographic characteristics should be preserved. The dolomitization of the aragonite (orthorhombic) is unlikely syntaxial, and the original growth zonations would also be destroyed (Hood and Wallace, 2012, 2018). Therefore, FSD and RSD in this study are likely primary minerals that directly precipitated from seawater during syn-sedimentary diagenesis (Tucker, 1982; Hood and Wallace, 2012; Wang et al., 2020). It should be noted that both length-slow and -fast dolomite cements have also been reported in the Dengying Formation from other

areas of South China (Hu et al., 2020; Zhao et al., 2021), in which the length-fast dolomite cements were explained as early dolomitization of the primary aragonite and high-Mg calcite.

Overall, MD and FD are products of the early mimetic dolomitization of primary minerals and syn-sedimentary direct dolomite precipitation respectively, which are distinct from the late-stage CD. The pervasive early dolomitization and syn-sedimentary dolomite cement precipitation in the Dengying Formation are consistent with recent studies on the Dengying Formation of the Yangtze Platform (Cui et al., 2019; Hu et al., 2020; Wang et al., 2020; Zhao et al., 2021), supporting the enhanced dolomitization and the possible presence of “aragonite-dolomite seas” at the late Ediacaran.

### 5.2. Preservation of coeval seawater chemical signals in dolomites

The Neoproterozoic syn-sedimentary early dolomitization and fibrous dolomite cement precipitation are proposed to be promoted by the peculiar coeval seawater chemistry (Hood and Wallace, 2018), and detailed geochemical investigations would provide useful insights into their formation environments (Hood and Wallace, 2012, 2018).

The REY concentrations and patterns of dolomites in our study demonstrate that they may preserve the coeval seawater chemistry. The REY data show low  $\sum$ REY concentrations (0.22–4.92 ppm, Table 1; Fig. 4C), which may lead to unreliable REY values and patterns, such as large Ce anomaly variations (0.22–1.97 ppm) (Li et al., 2019a). However, this possibility can be excluded by the uniform range of most Ce anomalies ( $1.0 \pm 0.3$  ppm) and the lack of co-variation between Ce anomaly and  $\sum$ REY (Fig. 4E). Furthermore, the poor correlations between Ce anomaly and Eu anomaly,  $(\text{Dy}/\text{Sm})_n$ ,  $\sum$ REY and  $(\text{La}/\text{Sm})_n$  ratios support the limited influence of diagenetic alternations on Ce anomaly (Fig. 4C–F), because diagenetic reactions would lead to the enrichment of Ce, depletion of Eu, and the decrease of  $(\text{Dy}/\text{Sm})_n$  and  $(\text{La}/\text{Sm})_n$  ratios (Nothdurft et al., 2004; Wang et al., 2020). The typical seawater-like progressive enrichment of heavy REY patterns is absent in all dolomite components investigated here. Instead, these dolomite components show flat to middle REY enriched patterns (Fig. 5). Such abnormal REY patterns may be influenced by detrital materials, which are usually high in REY concentrations and display flat patterns (Tostevin et al., 2016). However, the lack of correlations between Al concentrations and  $\sum$ REY,  $(\text{Nd}/\text{Yb})_n$  ratios excludes the potential influence of terrigenous materials (Fig. 4A–B). Conversely, the high Y/Ho ratios (34.6–330) and positive La anomalies (average 1.7) strongly suggest marine-sourced signals since seawater has high Y/Ho ratios and positive La anomalies compared to other environments (Fig. 5) (Tostevin et al., 2016). Therefore, MD and FD likely recorded primary REY signals with little alternations (Figs. 4–5). By contrast, the higher REY concentrations and larger Eu anomalies in CD suggest the potential influence of diagenetic exchanges and hydrothermal alternations during late-stage diagenesis (Figs. 4–5), because hydrothermal fluids present

**Table 2**

The elemental and C-O-Mg isotopic compositions of samples.

Sample	Height	Type	$\delta^{13}\text{C}$	SD	$\delta^{18}\text{O}$	SD	$\delta^{25}\text{Mg}$	2SD	$\delta^{26}\text{Mg}$	2SD	Mg/Ca	Sr/(Mg + Ca)	Mn/Sr	Na/(Mg + Ca)	K/(Mg + Ca)
	m		%	%	%	%	%	%	%	%	mol/mol	mmol/mol	mol/mol	mmol/mol	mmol/mol
YFP1-3	–	MD	2.69	0.05	-2.17	0.05									
YFP2-6	–	MD	3.70	0.04	-4.48	0.03									
YFP1-1	–	FD	3.24	0.07	-2.64	0.09									
YFP1-2	–	FD	3.65	0.12	-4.62	0.06	-1.11	0.01	-2.11	0.05	1.03	0.03	10.67	0.75	0.22
YFP1-4	–	FD	2.81	0.04	-3.80	0.06									
YFP2-1	–	FD	4.08	0.03	-2.93	0.06									
YFP2-2	–	FD	3.53	0.07	-4.15	0.07	-1.03	0.02	-1.98	0.03	1.05	0.04	23.49	0.88	0.23
YFP2-3	–	FD	3.94	0.07	-2.67	0.07									
YFP2-4	–	FD	2.83	0.03	-1.97	0.13									
YFP2-5	–	FD	3.58	0.01	-3.85	0.03									
GJS0-3-3	43.4	MD	2.26	0.08	-1.64	0.04	-1.15	0.05	-2.14	0.02	1.02	0.04	1.25	0.68	0.14
GJS0-3-5	43.4	MD	5.14	0.05	-2.04	0.05									
GJS0-3-6	43.4	MD	1.87	0.02	-2.91	0.03									
GJS1-1	41.4	MD	1.49	0.11	-4.04	0.16									
GJS1-2	41.4	MD	1.80	0.04	-1.99	0.02									
GJS2-2	39.4	MD	1.67	0.02	-1.66	0.03									
GJS3-4	37.4	MD	1.80	0.04	-3.15	0.04									
GJS3-8	37.4	MD	1.14	0.13	-7.64	0.14									
GJS3-10	37.4	MD	1.41	0.04	-3.91	0.05									
GJS4-3	5.8	MD	1.74	0.06	-4.93	0.03									
GJS6-1	9.7	MD	1.65	0.09	-4.60	0.16									
GJS8-1	15.7	MD	2.61	0.08	-5.02	0.10									
GJS9-6	18.7	MD	1.98	0.07	-4.32	0.09									
GJS10-5	22.4	MD	2.31	0.06	-3.60	0.05									
GJS11-6	26	MD	2.47	0.05	-3.82	0.07	-1.11	0.04	-2.10	0.09	1.04	0.03	2.51	0.71	0.20
GJS12-3	28.4	MD	1.44	0.10	-7.37	0.10									
GJS14-7	33.4	MD	1.86	0.09	-2.23	0.10									
GJS14-5	33.4	MD	1.86	0.09	-2.13	0.11									
GJS15-9	35.4	MD	1.72	0.06	-2.85	0.04	-0.86	0.02	-1.67	0.05	1.01	0.05	0.24	0.29	0.08
GJS1-7	41.4	FD	1.56	0.13	-3.63	0.09	-1.09	0.07	-2.11	0.07	1.03	0.05	1	0.74	0.23
GJS3-2	37.4	FD	1.51	0.12	-4.36	0.14	-1.06	0.02	-2.04	0.07	1.05	0.04	2.13	0.47	0.15
GJS5-1	7.1	FD	2.01	0.03	-4.01	0.05									
GJS8-2	15.7	FD	2.71	0.08	-0.79	0.09	-1.15	0.06	-2.22	0.09	1.03	0.03	1.42	1.30	0.32
GJS8-5	15.7	FD	2.37	0.06	-2.11	0.05	-1.13	0.04	-2.25	0.08	1.02	0.03	3.83	0.84	0.14
GJS9-2	18.7	FD	1.85	0.11	-4.71	0.09									
GJS10-4	22.4	FD	2.12	0.04	-2.12	0.03									
GJS11-4	26	FD	1.95	0.09	-6.20	0.09	-1.07	0.07	-2.04	0.01	1.03	0.03	5.95	0.34	0.11
GJS15-4	35.4	FD	1.13	0.07	-5.56	0.14	-1.05	0.06	-2.01	0.06	1.04	0.03	2.11	0.39	0.15
GJS15-10	35.4	FD	2.02	0.08	-3.05	0.07									
GJS5-3	7.1	CD	1.41	0.08	-11.48	0.10									
GJS6-3	9.7	CD	1.76	0.04	-5.43	0.05									
GJS7-1	13.7	CD	1.93	0.02	-1.47	0.04									
GJS8-6	15.7	CD	2.30	0.02	-3.14	0.02									
GJS11-1	26	CD	2.05	0.02	-8.43	0.03									
GJS15-6	35.4	CD	1.44	0.07	-2.92	0.06	-1.02	0.03	-1.96	0.02	1.02	0.04	1.70	0.20	0.08
YB1-1	3	MD	4.91	0.02	0.03	0.03									
YB1-2	3	MD	6.40	0.04	0.56	0.02									
YB3-1	6	MD	5.90	0.04	-0.11	0.05									
YB4-1	7	MD	1.21	0.06	-2.90	0.05									
YB5-2	9	MD	4.78	0.02	-2.76	0.02									
YB8-1	13	MD	5.78	0.10	-3.28	0.10									
YB8-3	13	MD	4.62	0.04	-1.73	0.04									
YB8-4	13	MD	5.94	0.03	-3.55	0.03									
YB19-2	30	MD	5.66	0.10	-4.08	0.12									
YB22-2	33	MD	4.99	0.05	-0.41	0.05									
YB22-4	33	MD	4.99	0.13	-5.07	0.12									
YB28-3	38	MD	4.45	0.10	-4.70	0.10									
YB34-2	42.5	MD	4.75	0.03	-2.87	0.03									
YB34-3	42.5	MD	3.42	0.04	-6.26	0.05									
YB36-3	45.5	MD	4.27	0.09	-1.40	0.07	-1.13	0.01	-2.17	0.07	1.04	0.09	0.18	2.08	0.30
YB36-4	45.5	MD	3.99	0.13	-1.73	0.08	-1.14	0.02	-2.14	0.09	1.04	0.10	0.20	2.40	0.28
YB45-3	61.2	MD	2.30	0.10	-6.19	0.12	-0.96	0.05	-1.85	0.00	1.04	0.05	4.00	1.02	0.14
YB46-4	65.2	MD	4.17	0.07	-2.54	0.06									
YB52-3	85.2	MD	3.70	0.05	-3.65	0.06									
YB56-2	91.7	MD	3.94	0.02	-1.40	0.03	-1.06	0.05	-2.05	0.09	1.03	0.03	3.02	1.29	0.22
YB59-2	99.7	MD	2.74	0.01	-3.46	0.02	-1.09	0.07	-2.10	0.05	1.04	0.03	5.07	1.40	0.21
YB64-1	118.7	MD	3.44	0.02	-4.25	0.02									
YB64-3	118.7	MD	3.55	0.03	-3.51	0.04									
YB66-1	135.2	MD	3.36	0.02	-7.43	0.03									
YB66-3	135.2	MD	3.53	0.02	-4.16	0.04									

(continued on next page)

**Table 2 (continued)**

Sample	Height	Type	$\delta^{13}\text{C}$	SD	$\delta^{18}\text{O}$	SD	$\delta^{25}\text{Mg}$	2SD	$\delta^{26}\text{Mg}$	2SD	Mg/Ca	Sr/(Mg + Ca)	Mn/Sr	Na/(Mg + Ca)	K/(Mg + Ca)
	m		‰	‰	‰	‰	‰	‰	‰	‰	mol/mol	mmol/mol	mol/mol	mmol/mol	mmol/mol
YB67-3	143.2	MD	3.57	0.06	-4.09	0.05	-1.11	0.01	-2.08	0.04	1.03	0.04	2.70	0.97	0.19
YB74-3	164.7	MD	3.93	0.02	-3.52	0.02									
YB80-1	218.7	MD	2.73	0.07	-0.88	0.06									
YB81-1	219.7	MD	3.34	0.06	-2.45	0.08									
YB83-3	226.2	MD	1.89	0.04	-4.22	0.02	-1.04	0.05	-1.96	0.07	1.05	0.04	1.96	0.60	0.16
YB83-1-3	226.2	MD	2.37	0.03	-4.70	0.01									
YB83-1-2	226.2	MD	2.54	0.06	-5.29	0.06									
YB19-4	30	FD	5.62	0.06	-3.59	0.05	-1.00	0.03	-1.92	0.06	1.02	0.05	2	1.12	0.23
YB22-1	33	FD	5.41	0.08	-2.41	0.06									
YB22-3	33	FD	5.04	0.08	-1.58	0.09	-1.08	0.03	-2.09	0.06	1.03	0.04	2.15	1.08	0.23
YB26-3	35.5	FD	4.89	0.10	-3.77	0.11	-1.07	0.07	-2.07	0.03	1.05	0.09	1.12	1.49	0.17
YB28-1	38	FD	4.08	0.12	-7.91	0.11	-0.85	0.04	-1.64	0.08	1.02	0.05	7.87	0.46	0.10
YB45-2	61.2	FD	2.54	0.13	-6.89	0.05	-0.92	0.05	-1.81	0.09	1.03	0.04	8.14	0.71	0.31
YB45-5	61.2	FD	2.45	0.11	-4.10	0.05	-0.98	0.04	-1.91	0.04	1.03	0.05	8.36	0.70	0.30
YB49-1	81.7	FD	1.85	0.02	-4.54	0.02	-1.08	0.08	-2.08	0.08	1.03	0.03	2.06	1.11	0.31
YB52-1	85.2	FD	3.96	0.04	-7.15	0.06									
YB56-1	91.7	FD	2.94	0.04	-6.88	0.03									
YB56-3	91.7	FD	3.36	0.02	-1.88	0.03	-1.01	0.04	-1.98	0.05	1.04	0.03	3.55	1.08	0.10
YB59-3	99.7	FD	2.83	0.04	-1.85	0.06									
YB60-1	109.7	FD	3.26	0.05	-1.28	0.05									
YB60-3	109.7	FD	3.59	0.05	-2.54	0.04									
YB60-4	109.7	FD	2.94	0.05	-3.40	0.09									
YB67-2	143.2	FD	3.53	0.06	-3.43	0.05	-1.14	0.08	-2.16	0.05	1.03	0.04	2.10	1.21	0.22
YB67-4	143.2	FD	3.40	0.03	-2.99	0.01	-1.08	0.03	-2.01	0.04	1.04	0.03	2.85	0.98	0.18
YB74-2	164.7	FD	3.30	0.04	-2.11	0.05									
YB83-4	226.2	FD	1.99	0.04	-2.68	0.05	-1.06	0.03	-2.05	0.03	1.03	0.03	2.67	1.27	0.16
YB83-5	226.2	FD	1.65	0.01	-4.56	0.02	-1.02	0.04	-1.92	0.07	1.02	0.03	3.34	1.05	0.21
YB26-2	38	CD	2.85	0.17	-11.25	0.12	-1.03	0.07	-2.00	0.06	1.06	0.04	22	0.21	0.10
YB28-2	38	CD	4.00	0.10	-10.13	0.07									
YB28-4	35.5	CD	4.46	0.10	-9.99	0.08									
YB34-1	42.5	CD	4.52	0.02	-4.11	0.04									
YB45-6	61.2	CD	2.19	0.08	-9.65	0.03	-0.97	0.00	-1.90	0.01	1.05	0.05	20.81	0.57	0.15
YB49-4	81.7	CD	1.97	0.06	-8.08	0.05									
YB52-2	85.2	CD	3.71	0.05	-7.12	0.04									
YB59-1	99.7	CD	2.42	0.07	-7.57	0.06	-1.06	0.01	-2.02	0.05	1.06	0.03	10.79	0.61	0.11
YB60-2	109.7	CD	2.93	0.05	-8.84	0.06									
YB64-2	118.7	CD	3.28	0.06	-5.97	0.07									
YB66-2	135.2	CD	3.01	0.05	-3.33	0.05									
YB67-1	143.2	CD	3.08	0.05	-9.52	0.06	-1.02	0.05	-1.96	0.04	1.06	0.07	3.34	0.31	0.10
YB69-2	150.7	CD	3.47	0.05	-0.92	0.05									
YB74-1	164.7	CD	3.06	0.04	-9.14	0.04									
YB80-2	218.7	CD	2.53	0.04	-3.30	0.04									
YB83-6	226.2	CD	1.93	0.02	-7.08	0.03	-0.94	0.02	-1.77	0.02	1.04	0.03	13.59	0.51	0.09
YB83-1-1	226.2	CD	2.39	0.08	-7.54	0.05									

pronounced positive Eu anomalies (Tostevin et al., 2016). These REY characteristics in CD are consistent with its coarse crystal sizes and the lack of sedimentary fabrics (Fig. 3), as well as findings in recent studies (Hu et al., 2020; Wang et al., 2020). The absence of Ce anomalies (mostly  $1.0 \pm 0.3$ ) in MD and FD indicates a probable anoxic seawater condition during the precipitation of dolomites at the basal Dengying Formation because Ce (III) would be oxidized to Ce (IV) and absorbed into Fe-Mn oxides in oxic seawater and thus produces negative Ce anomalies (Moffett, 1994). Similar Ce anomalies and anoxic conditions in the Algal Dolomite Member have been documented previously in southern Shaanxi Province and adjacent regions (Wang et al., 2020; Zhao et al., 2020). Meanwhile, bulk and *in situ* carbonate REY analyses of the Dengying Formation from the Yangtze Gorges area and Southeast Sichuan displayed slightly negative Ce anomalies (Ling et al., 2013; Hu et al., 2020). The shallow marine anoxia is likely transient and regionally restricted in the global context of the late Neoproterozoic oxygenation.

Moreover, we suggest that MD and FD recorded the coeval seawater C and O isotope signatures for the following reasons. First, the C and O isotopic compositions of MD and FD from the GJS section are similar to a

chemostratigraphic study from the same site (Cui et al., 2019). The  $\delta^{13}\text{C}$  values of samples in the YB section show a similar range to the general  $\delta^{13}\text{C}$  trends at the latest Ediacaran in South China (Zhu et al., 2007). Furthermore, MD and FD from both GJS and YB sections also show relatively high ( $> -6\text{‰}$ ) and comparable  $\delta^{18}\text{O}$  values with previous studies (Fig. 6) (Cui et al., 2019; Wang et al., 2020), suggesting limited diagenetic alterations. These isotopic characteristics demonstrate that these two dolomite components were precipitated from the terminal Ediacaran seawater with negligible post-depositional alterations (Fig. 6). By contrast, CD displays low  $\delta^{18}\text{O}$  values down to  $\sim -12\text{‰}$  (Fig. 6B and E), indicating significant diagenetic alterations from meteoric waters or deep burial (Kaufman and Knoll, 1995; Derry, 2010; Swart, 2015).

The correlations between  $\delta^{26}\text{Mg}$  values and Mn/Sr ratios,  $\delta^{18}\text{O}$  values may indicate the potential effect of meteoric diagenesis on Mg isotopic compositions (Fig. 7A–B). Nevertheless, freshwater usually has higher C and O contents than Mg, thus the Mg isotope compositions of dolomites are unlikely to be altered by meteoric diagenesis when the C and O isotope compositions are largely pristine. Furthermore, the roughly increasing Sr/(Mg + Ca) ratios in samples with higher  $\delta^{26}\text{Mg}$

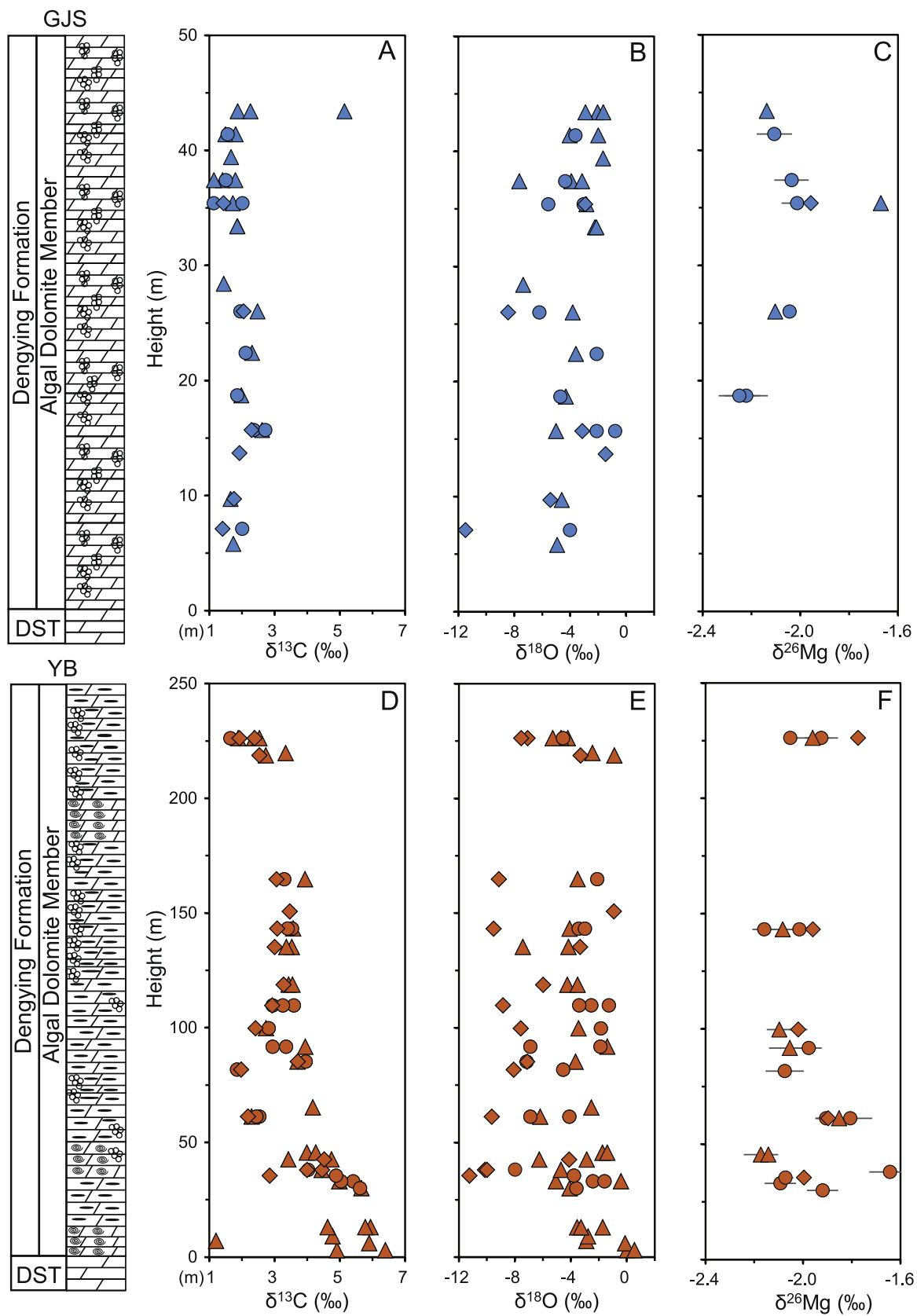
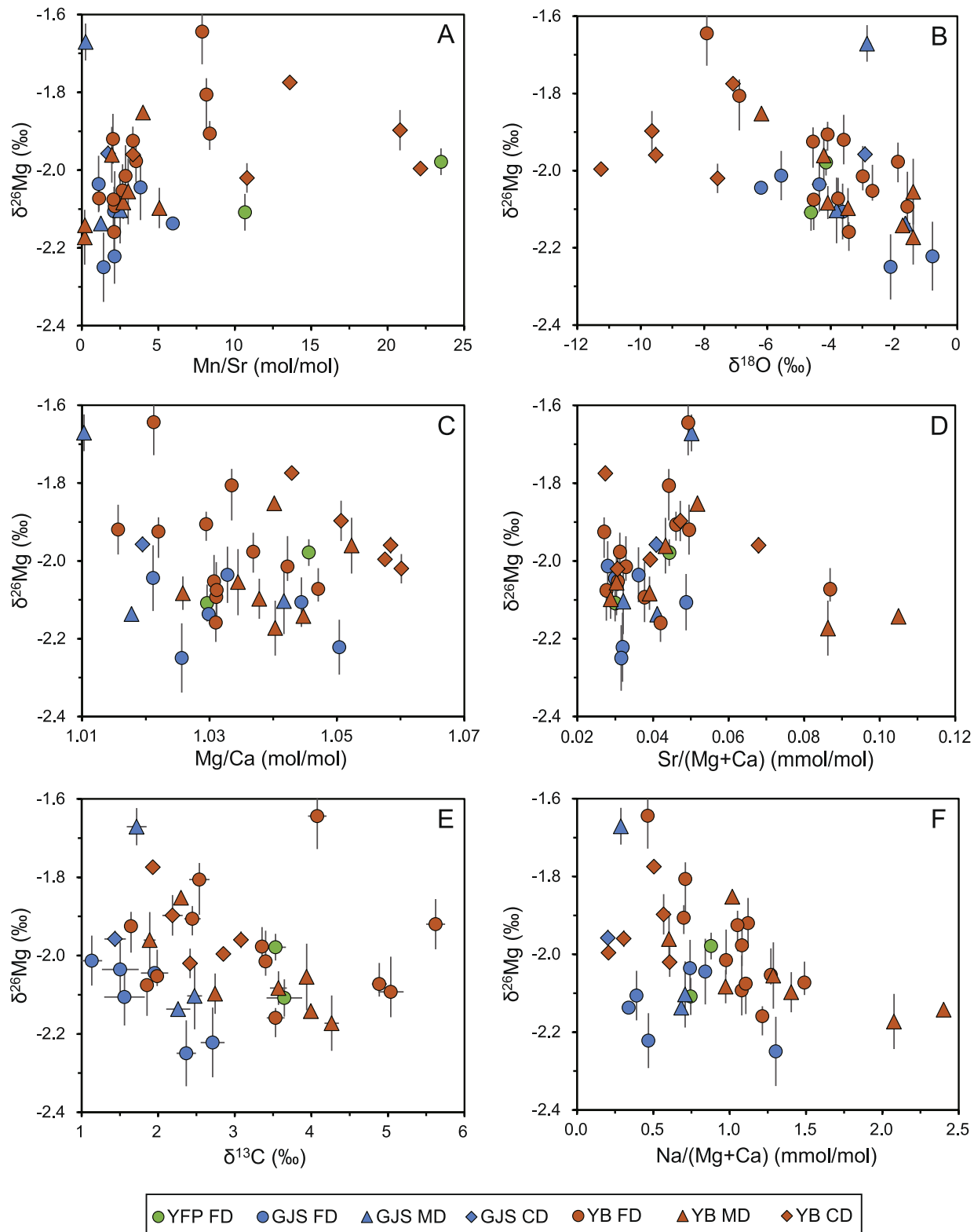


Fig. 6. The C-O-Mg isotope stratigraphy of the GJS and YB sections respectively, the legend and age constraints are as same as Fig. 1.



**Fig. 7.** Crossplots of  $\delta^{26}\text{Mg}$  versus Mn/Sr,  $\delta^{18}\text{O}$  values, Mg/Ca, Sr/(Mg + Ca),  $\delta^{13}\text{C}$  and Na/(Mg + Ca) ratios of MD, FD, and CD from the GJS, YFP, and YB sites. Error bars mean two times standard deviations.

values also exclude the enrichment of heavy Mg isotopes as the increase of Mn/Sr ratios (Fig. 7A and D), because generally Sr would be lost during diagenesis. Additionally, the  $\delta^{26}\text{Mg}$  variations cannot be generated from the inheritance of precursors or recrystallization since the high and homogeneous Mg/Ca ratios in dolomites indicate the complete

dolomitization and near stoichiometric dolomites (Fig. 7C). Moreover, if the heavy Mg isotopic compositions in dolomites are indicative of aragonite precursors, these samples should have high Na/(Mg + Ca) and K/(Mg + Ca) ratios, which is inconsistent with our results (Figs. 7F and 8D). Most importantly, the fine-grained MD and FD show no evidence of

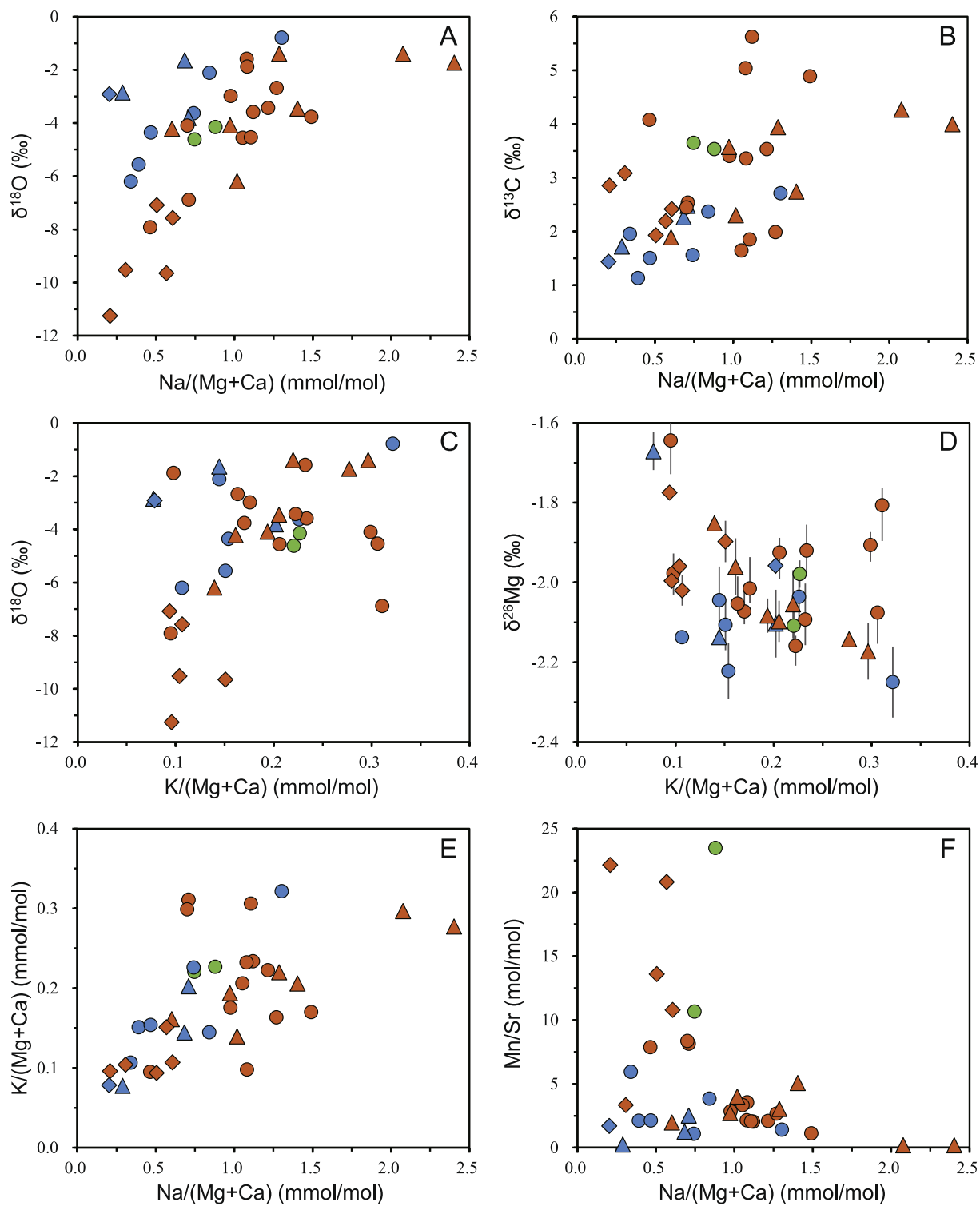


**Fig. 8.** Crossplots of  $\text{Na}/(\text{Mg} + \text{Ca})$  versus  $\delta^{18}\text{O}$  and  $\delta^{13}\text{C}$  values (A–B),  $\text{K}/(\text{Mg} + \text{Ca})$  versus  $\delta^{18}\text{O}$  and  $\delta^{26}\text{Mg}$  (C–D), and  $\text{Na}/(\text{Mg} + \text{Ca})$  versus  $\text{K}/(\text{Mg} + \text{Ca})$  and  $\text{Mn/Sr}$  ratios (E–F). Error bars mean two times standard deviations.

recrystallization (Fig. 3), and the enlarged CD only has marginally elevated  $\delta^{26}\text{Mg}$  values (Fig. 7). Overall, Mg isotope compositions of MD and FD are not influenced by post-depositional processes, instead, they largely preserved the initial isotopic records of seawater from which dolomites were formed. The relatively narrow  $\delta^{26}\text{Mg}$  ranges ( $\sim 0.6\text{\textperthousand}$ ) of both MD and FD from the two sections reflect that they were formed in shallow marine sediments (Mavromatis et al., 2014; Higgins et al., 2018), and their similar  $\delta^{26}\text{Mg}$  ranges and values in MD and FD imply

these two components were largely formed in the same marine context (Fig. 6). By contrast, slightly elevated average  $\delta^{26}\text{Mg}$  values ( $\sim 0.1\text{\textperthousand}$ ) in CD likely indicate the influence of deep burial diagenesis, since hydrothermal-altered dolomites showed slightly increased Mg isotope compositions (Azmy et al., 2013). The marginal increase of  $\delta^{26}\text{Mg}$  in the severely-altered CD component further demonstrates the resistance of Mg isotope signatures in dolomites and the preservation of initial isotopic fingerprints in MD and FD.

### 5.3. Constraining the seawater Mg/Ca variation

Because the Mg isotopic compositions of MD and FD components in dolostones of the lower Algal Dolomite Member in Dengying Formation were well exchanged with the coeval seawater and largely immune to post-depositional alternations, their noticeable variations (~0.6‰) likely reflect the heterogeneity of the precipitating fluid. A possible scenario is the widespread mixture of freshwater and seawater in the shallow platform settings by increased riverine input according to the negatively correlated  $\delta^{18}\text{O}$  and  $\delta^{26}\text{Mg}$  values (Fig. 7B). Freshwater usually has lighter O isotope compositions, and lower Na and K concentrations compared to seawater, hence lower  $\delta^{18}\text{O}$  values, Na/(Mg + Ca) and K/(Mg + Ca) ratios can be used as indicators of freshwater-dominated endmember. Relatively lower Na/(Mg + Ca) and K/(Mg + Ca) ratios,  $\delta^{13}\text{C}$  and  $\delta^{18}\text{O}$  values observed in dolomites suggest higher proportions of freshwater in the precipitating fluid (Figs. 7–8), and the variations of these geochemical parameters likely mirror the addition of various proportions freshwater in the coeval seawater (Figs. 7–8). Considering the relatively restricted settings and very shallow platform reefal and shoal facies during the carbonate deposition of the Dengying Formation (Cui et al., 2019; Hu et al., 2020), it is plausible that the platform seawater was influenced by the increased fluvial input at the basal Dengying Formation. Furthermore, the freshwater endmember with lower  $\delta^{18}\text{O}$  values, Na/(Mg + Ca) and K/(Mg + Ca) ratios tend to have heavier Mg isotope compositions (Figs. 7–8), indicating the fluvial input has isotopically heavier Mg than that of the seawater. The heavier Mg isotopic compositions in freshwater endmember reflect a silicate-dominated weathering flux, because rivers that drain silicate rocks have higher  $\delta^{26}\text{Mg}$  values than both seawater and rivers draining carbonate rocks (Tipper et al., 2006). The negative correlations between  $\delta^{26}\text{Mg}$  and  $\delta^{13}\text{C}$  further support this inference (Fig. 7E), since silicate-dominated weathering flux tends to have lighter C isotopic compositions and higher  $\delta^{26}\text{Mg}$  values (Pokrovsky et al., 2011).

Similar influences of silicate weathering flux on Mg isotopic compositions of shallow marine settings have been documented in a series of Neoproterozoic successions (Pokrovsky et al., 2011; Kasemann et al., 2014; Liu et al., 2014, 2018), and the increased weathering flux would substantially affect the seawater chemistry and last from thousands of years to several million years on a regional to global scale (Pokrovsky et al., 2011; Kasemann et al., 2014; Liu et al., 2014, 2018). The enhanced (silicate) weathering flux has also been widely reported in the late Ediacaran biomineralized fossils bearing strata in South China (Sawaki et al., 2010; Cui et al., 2016), Namibia (Ries et al., 2009), Siberia (Wood et al., 2017a), and Brazil (Paula-Santos et al., 2020), and here our data suggest that this enhanced silicate-dominated weathering likely started ahead of the earliest animal biomimeticization. Generally, silicate-dominated weathering flux would have obviously higher Mg/Ca ratios than that of the modern mixed fluxes (0.78 vs. 0.39, Wilkinson and Algeo, 1989). Since riverine input is the main Mg source of the oceans, increased silicate-dominated weathering flux during the terminal Ediacaran may substantially influence the coeval chemical composition of seawater. Assuming a constant Ca flux, the high Mg/Ca ratio in silicate-dominated riverine input means the flux of Mg could be nearly doubled. The effect of this silicate-dominated weathering flux on seawater Mg/Ca ratio and  $\delta^{26}\text{Mg}$  can be simply modeled using the following mass balance equations:

$$\frac{dN_{\text{Mg}}}{dt} = F_{\text{riv}} - F_{\text{dol}} - F_{\text{MOR}} \quad (6)$$

$$\frac{N_{\text{Mg}} d(\delta^{26}\text{Mg}_{\text{sw}})}{dt} = \delta^{26}\text{Mg}_{\text{riv}} \times F_{\text{riv}} - (\delta^{26}\text{Mg}_{\text{sw}} - \Delta^{26}\text{Mg}_{\text{dol-sw}}) \times F_{\text{dol}} - (\delta^{26}\text{Mg}_{\text{sw}} - \Delta^{26}\text{Mg}_{\text{MOR-sw}}) \times F_{\text{MOR}} \quad (7)$$

The variation of total Mg in the oceans ( $N_{\text{Mg}}$ ), is determined by the input of Mg from rivers ( $F_{\text{riv}}$ ) and the outputs of Mg during dolomitization ( $F_{\text{dol}}$ ) and mid-ocean ridge reactions ( $F_{\text{MOR}}$ ), and the variation of

seawater Mg isotopic composition ( $\delta^{26}\text{Mg}_{\text{sw}}$ ) is determined by changes in flux and Mg isotopic signatures of Mg inputs and outputs. The dolomitization flux during this period can be supposed as same as that during the Terreneuvian (~43% of the total carbonate, Li et al., 2021), considering the abundant dolomite formation in the Dengying Formation of the Yangtze Platform, and the Yudoma Group of the Siberian Platform (Wood et al., 2017b). This means the flux of Mg via dolomitization could be set as  $7.91 \times 10^{12}$  mol/yr, about three times of modern flux (Wilkinson and Algeo, 1989). The Mg isotope fractionation during dolomitization and mid-ocean ridge reactions can be estimated as ~1.8‰ and 0.8‰ (Li et al., 2015; Huang et al., 2018), and  $\delta^{26}\text{Mg}$  of the silicate-dominated and mixed flux of riverine input can be set as ~−0.2‰ and ~−1.1‰ respectively (Tipper et al., 2006). The detailed parameters used in the model can be found in Table 3.

Results show that the enhanced dolomitization during this period would significantly promote the removal of Mg from seawater, resulting in a dramatic drop of seawater Mg/Ca ratio (drop by ~1.5 within 3 Myr, Fig. 9A–B). At the same time, the silicate-dominated weathering flux from the basal Dengying Formation would deliver more Mg to oceans to buffer this enhanced Mg removal (Fig. 9A–B). Consequently, the seawater Mg/Ca ratio would decrease slightly or remain invariable during this period (Fig. 9A–B). The corresponding  $\delta^{26}\text{Mg}_{\text{sw}}$  would be increased by ~0.5‰ and ~0.75‰ if the seawater Mg/Ca ratio is set as 6 and 4 at ~548 Ma respectively (Fig. 9C–D). Considering the positive dolomite  $\delta^{26}\text{Mg}$  excursion at the Ediacaran-Cambrian boundary (~2‰, Pokrovsky et al., 2011; Stammeier et al., 2020), the seawater Mg/Ca ratio of 4 and 6 at ~548 Ma both meet the geological record since the increase in silicate weathering flux and dolomitization would likely weaken in upper successions in the following ~10 Myr. It is not surprising that this increasing stratigraphic trend is not observed in Fig. 6, since our samples just cover the basal Algal Dolomite Member. Therefore, the dolomite  $\delta^{26}\text{Mg}$  records support the enhanced silicate weathering influx at the terminal Ediacaran (Pokrovsky et al., 2011; Stammeier et al., 2020), and this silicate-dominated weathering flux may fundamentally influence the chemical condition of the oceans on the eve of the early animal biomimeticization.

### 5.4. Implications for the onset of metazoan biomimeticization

Constraining the terminal Ediacaran seawater chemistry and its variation is crucial for understanding the co-evolution between environment and life since significant changes in tectonic, climatic, geochemical, and biological processes simultaneously occurred during this critical period (Li et al., 2013; Bowyer et al., 2017; Wood, 2018; Stammeier et al., 2019; Zhou et al., 2019; Chen et al., 2021). The enhanced silicate weathering at the eve of the earliest animal biomimeticization is likely related to these Earth's surface changes. During the assemblage of the Gondwana, widespread collisions of continents and large orogens and uplift potentially provided abundant eroded silicate rocks for chemical weathering throughout the late Ediacaran (Peters and Gaines, 2012; Li et al., 2013; Yao et al., 2021), which is indicated by the increased radioactive Sr isotopes in seawater (Stammeier et al., 2019, 2020; Chen et al., 2021). Moreover, although there are no diamictite records in South China, the late Ediacaran Gaskiers Glaciation in nearby and worldwide blocks, such as Hankalchough in Tarim and Luoquan in North China (Zhou et al., 2019), indicate the South China Block might be influenced by abundant weathering materials or meltwater generated by the Glaciation. Therefore, the exposed pulverized silicate-dominated rocks produced by the final assembly of the Gondwana and the glacier erosion would facilitate the chemical weathering of silicate rocks under a warm climate backdrop during the terminal Ediacaran, which is supported by the heavy Mg isotopic signatures in marine carbonates and continental shales at the Ediacaran-Cambrian transition (Pokrovsky et al., 2011; Stammeier et al., 2020; Zhang et al., 2021). The abundant cations and alkalinity in the silicate-dominated weathering flux would be delivered to the oceans, contributing to the geochemical

**Table 3**  
Parameters used in the mass balance model.

	Parameters	Value	Reference
Constant Mg flux	$N_{Mg}$ at $\sim 548$ Ma	$6(4) \times 10^{19}$ mol	Wilkinson and Algeo, 1989; Horita et al., 2002; Brennan et al., 2004
	$\delta^{26}Mg_{sw}$ at $\sim 551$ Ma	-0.4‰	This study
	$F_{riv}$	$5.2 \times 10^{12}$ mol/yr	Wilkinson and Algeo, 1989
	$\delta^{26}Mg_{riv}$	-1.10‰	Tipper et al., 2006
Increased value	$F_{dol}$	$2.6 \times 10^{12}$ mol/yr	Wilkinson and Algeo, 1989
	$\delta^{26}Mg_{dol}$	$\delta^{26}Mg_{sw} - 1.8\text{‰}$	Li et al., 2015
	$F_{MOR}$	$2.6 \times 10^{12}$ mol/yr	Wilkinson and Algeo, 1989
	$\delta^{26}Mg_{MOR}$	$\delta^{26}Mg_{sw} + 0.8\text{‰}$	Huang et al., 2018
Increased value	Increased $F_{riv}$	$10.3 \times 10^{12}$ mol/yr	Wilkinson and Algeo, 1989
	Increased $\delta^{26}Mg_{riv}$	-0.2‰	Tipper et al., 2006
	Increased $F_{dol}$	$7.91 \times 10^{12}$ mol/yr	Wilkinson and Algeo, 1989; Li et al., 2021

The amount of Mg in the oceans  $N_{Mg}$  at  $\sim 548$  Ma is estimated as 6 and  $4 \times 10^{19}$  mol respectively to simulate the seawater Mg/Ca ratio of 6 and 4. The  $\delta^{26}Mg_{sw}$  at  $\sim 551$  Ma is estimated based on the seawater-dominated endmember in our samples. The  $F_{MOR}$  and the oceanic Ca budget are assumed to be constant for easy calculation of the seawater Mg/Ca ratio variation. The Mg isotopic compositions of dolomite and altered mid-ocean ridge depend on the dynamic  $\delta^{26}Mg_{sw}$  with fixed fractionation factors relative to the seawater. Constant Mg flux parameters are set as modern values and remain constant during the period of  $\sim 551$  to  $\sim 548$  Ma. Increased value: parameters are adjusted to simulate the silicate-dominated weathering flux and enhanced dolomitization during the modeled duration.

heterogeneity in dolomites from the basal Dengying Formation.

The enhanced silicate-dominated weathering input at the basal Dengying Formation likely provided a habitable marine environment for the closely followed earliest animal biomineralization. On the one hand,

silicate-dominated weathering flux would deliver flux with higher Mg/Ca ratios than the mixed weathering flux to the oceans and counteract the enhanced removal of Mg by dolomitization, maintaining a relatively stable and high Mg/Ca ratio (probably around 6 or 4) in the oceans. The

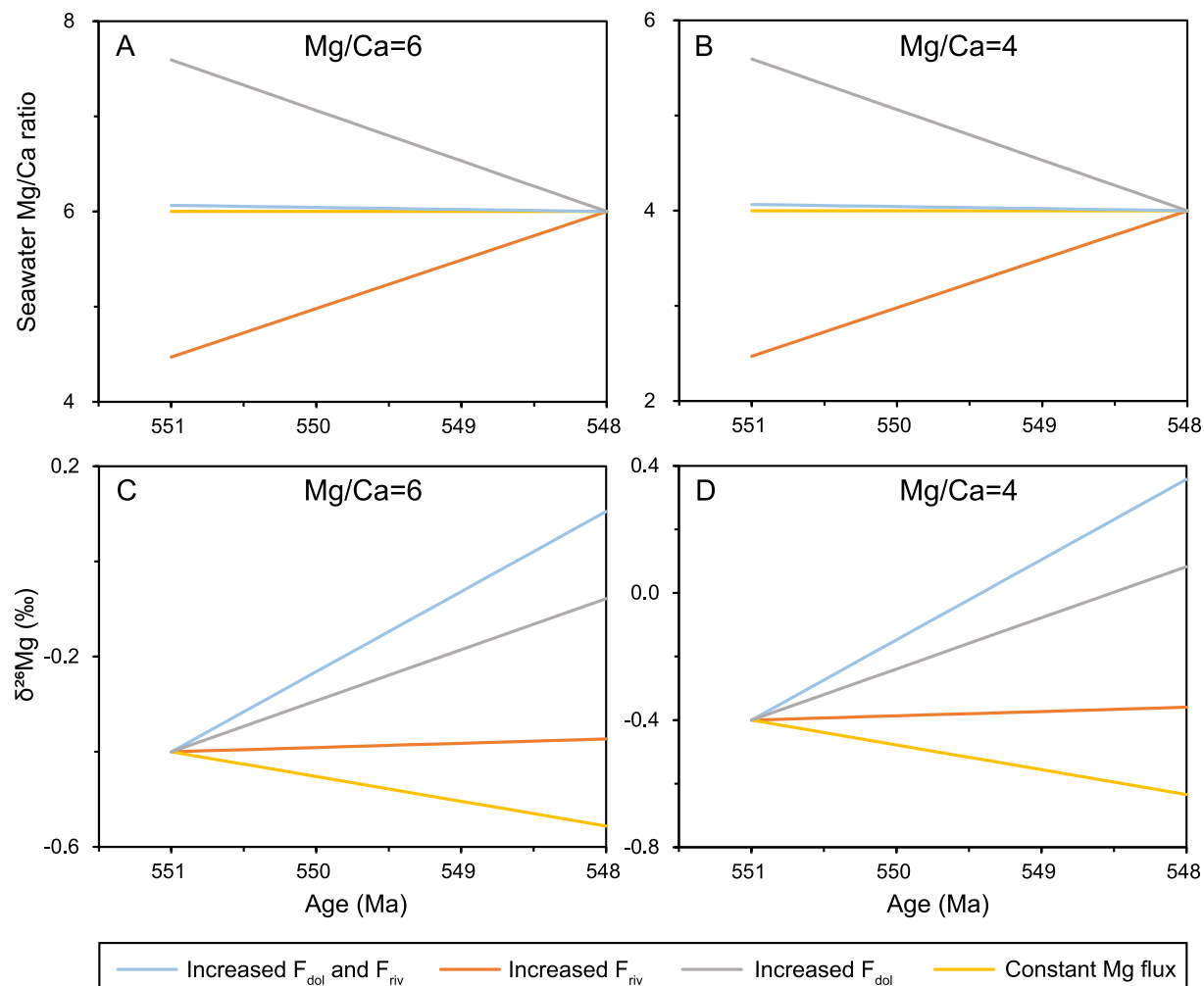


**Fig. 9.** Responses of seawater Mg/Ca ratio (A–B) and Mg isotopic composition (C–D) to enhanced dolomitization and silicate-dominated weathering flux within a duration of  $\sim 3$  Ma at the terminal Ediacaran, and the seawater Mg/Ca ratio at  $\sim 548$  Ma is set as 6 (A and C) and 4 (B and D) respectively. The effect of increased dolomitization, silicate-dominated riverine input, and both were considered in the model and compared to the constant oceanic Mg budget. Detailed parameters can be seen in Table 3.

relatively high seawater Mg/Ca ratio is consistent with the dominated aragonite skeletons in the terminal Ediacaran oceans (Wood, 2018). On the other hand, silicate weathering could deliver more net alkalinity to the oceans that carbonate would not, and the enhanced alkalinity would increase the carbonate saturation on a geological timescale for the subsequent bio-calcifying. Investigations on calcified skeleton bearing strata during this interval indicate the terminal Ediacaran oceans were highly alkaline (Cui et al., 2016; Wood et al., 2017a; Paula-Santos et al., 2020), and this high alkalinity may be partially generated by the increased silicate weathering flux at the basal Dengying Formation. Therefore, a relatively high Mg/Ca ratio and accumulated alkalinity in marine settings set the stage for the innovative calcification of the early animals ahead of its occurrence. The duration of this enhanced silicate-dominated weathering flux is unknown, while it may contribute to the protracted relatively high seawater Mg/Ca ratio at the Ediacaran-Cambrian transition (Horita et al., 2002; Brennan et al., 2004), and the increased Ca concentration and decreased seawater Mg/Ca ratio in the early Cambrian may involve its weakening (Brennan et al., 2004).

## 6. Conclusions

To constrain the seawater chemistry on the eve of metazoan biomineralization, systematic sedimentological, petrographic, trace elemental, and C-O-Mg isotopic investigations were conducted on botryoidal dolomites from the Algal Dolomite Member of the terminal Ediacaran Dengying Formation. Dolostones from the Algal Dolomite Member developed massive botryoidal dolomites, including microbialites, fibrous dolomite cements, and void-filling crystalline dolomite cements. Microbialites show well-preserved finely crystallized sedimentary structures, indicating early mimetic dolomitization of precursor minerals. The elaborate isopachous growth zones and cathodoluminescence bands preserved in fibrous dolomite cements reflect a syn-sedimentary shallow marine origin. These abundant syn-sedimentary dolomites suggest the presence of “aragonite-dolomite seas” in the latest Ediacaran, and their trace elements revealed a relatively anoxic shallow marine setting. The correlated  $\delta^{26}\text{Mg}$  and  $\delta^{18}\text{O}$  values, and elemental ratios in dolomites further reveal the pervasive mixture of freshwater and seawater in the shallow platform, which reflects enhanced riverine input. Specifically, this riverine input should be dominated by silicate weathering flux due to its higher  $\delta^{26}\text{Mg}$  values. The silicate-dominated weathering flux may be related to the tectonic and climatic changes during the terminal Ediacaran, and it would deliver more Mg cations and net alkalinity to the oceans than the mixed weathering flux. Consequently, this silicate-dominated weathering flux likely played significant roles in maintaining a relatively high seawater Mg/Ca ratio and enhancing the carbonate supersaturation, and further facilitated the subsequent animal biomineralization and influenced the polymorphism of their skeletons.

## CRediT authorship contribution statement

**Pan Zhang:** Methodology, Validation, Visualization, Writing – review & editing. **Kang-Jun Huang:** Conceptualization, Supervision, Validation, Visualization, Project administration, Writing – review & editing. **Mao Luo:** Conceptualization, Supervision, Visualization, Project administration, Writing – review & editing. **Yaoping Cai:** Visualization, Writing – review & editing. **Zhian Bao:** Visualization, Methodology.

## Declaration of Competing Interest

The authors declare that they have no known competing financial interests or personal relationships that could have appeared to influence the work reported in this paper.

## Acknowledgements

We thank Dr. Zhongwu Lan for his editorial handling. We also thank Dr. Xinqiang Wang and one anonymous reviewer for their constructive comments, which significantly improved this manuscript. This study is financially supported by National Natural Science Foundation of China (No. 41973008, 41890845, 42072004 and 42130206), and the Strategic Priority Research Program of Chinese Academy of Sciences (No. XDB26000000). M.L. was funded by the Chinese Academy of Sciences Talents Program (2018-039).

## References

- Azmy, K., Lavoie, D., Wang, Z., Brand, U., Al-Aasm, I., Jackson, S., Girard, I., 2013. Magnesium-isotope and REE compositions of Lower Ordovician carbonates from eastern Laurentia: Implications for the origin of dolomites and limestones. *Chem. Geol.* 356, 64–75.
- Banerjee, A., Slowakiewicz, M., Majumder, T., Khan, S., Patranabis-Deb, S., Tucker, M.E., Saha, D., 2019. A Palaeoproterozoic dolomite (Vempalle Formation, Cuddapah Basin, India) showing Phanerozoic-type dolomitisation. *Precambr. Res.* 328, 9–26.
- Bao, Z., Huang, K., Huang, T., Shen, B., Zong, C., Chen, K., Yuan, H., 2019. Precise magnesium isotope analyses of high-K and low-Mg rocks by MC-ICP-MS. *J. Anal. At. Spectrom.* 34 (5), 940–953.
- Bialik, O.M., Wang, X., Zhao, S., Waldmann, N.D., Frank, R., Li, W., 2018. Mg isotope response to dolomitization in hinterland-attached carbonate platforms: Outlook of  $\delta^{26}\text{Mg}$  as a tracer of basin restriction and seawater Mg/Ca ratio. *Geochim. Cosmochim. Acta.* 235, 189–207.
- Bowyer, F., Wood, R.A., Poulton, S.W., 2017. Controls on the evolution of Ediacaran metazoan ecosystems: A redox perspective. *Geobiology* 15 (4), 516–551.
- Brennan, S.T., Lowenstein, T.K., Horita, J., 2004. Seawater chemistry and the advent of biocalcification. *Geology* 32 (6), 473. <https://doi.org/10.1130/G20251.110.1130/2004082>.
- Cai, Y., Hua, H., Xiao, S., Schiffbauer, J.D., Li, P., 2010. Biostratinomy of the late Ediacaran pyritized Gaojiashan Lagerstätte from southern Shaanxi, South China: importance of event deposits. *Palaios* 25 (8), 487–506.
- Cai, Y., Xiao, S., Li, G., Hua, H., 2019. Diverse biomineralizing animals in the terminal Ediacaran Period herald the Cambrian explosion. *Geology* 47 (4), 380–384.
- Chen, X.I., Zhou, Y., Shields, G.A., 2022. Progress towards an improved Precambrian seawater  $^{87}\text{Sr}/^{86}\text{Sr}$  curve. *Earth-Science Reviews* 224, 103869. <https://doi.org/10.1016/j.earscirev.2021.103869>.
- Condon, D., Zhu, M., Bowring, S., Wang, W., Yang, A., Jin, Y., 2005. U-Pb Ages from the Neoproterozoic Doushantuo Formation, China. *Science* 308 (5718), 95–98.
- Cui, H., Kaufman, A.J., Xiao, S., Peek, S., Cao, H., Min, X., Cai, Y., Siegel, Z., Liu, X.-M., Peng, Y., Schiffbauer, J.D., Martin, A.J., 2016. Environmental context for the terminal Ediacaran biomineralization of animals. *Geobiology* 14 (4), 344–363.
- Cui, H., Xiao, S., Cai, Y., Peek, S., Plummer, R.E., Kaufman, A.J., 2019. Sedimentology and chemostratigraphy of the terminal Ediacaran Dengying Formation at the Gaojiashan section, South China. *Geol. Mag.* 156 (11), 1924–1948.
- Derry, L.A., 2010. A burial diagenesis origin for the Ediacaran Shuram-Wonoka carbon isotope anomaly. *Earth. Planet. Sci. Lett.* 294 (1–2), 152–162.
- Ding, Y.i., Chen, D., Zhou, X., Guo, C., Huang, T., Zhang, G., Brasier, A., 2019. Cavity-filling dolomite speleothems and submarine cements in the Ediacaran Dengying microbialites, South China: Responses to high-frequency sea-level fluctuations in an ‘aragonite-dolomite sea’. *Sedimentology* 66 (6), 2511–2537.
- Hardie, L.A., 1996. Secular variation in seawater chemistry: An explanation for the coupled secular variation in the mineralogies of marine limestones and potash evaporites over the past 600 m.y. *Geology* 24 (3), 279–283.
- Hardie, L.A., 2003. Secular variations in Precambrian seawater chemistry and the timing of Precambrian aragonite seas and calcite seas. *Geology* 31 (9), 785. <https://doi.org/10.1130/G19657.110.1130/2003114>.
- Higgins, J.A., Blättler, C.L., Lundstrom, E.A., Santiago-Ramos, D.P., Akhtar, A.A., Crüger Ahm, A.-S., Bialik, O., Holmden, C., Bradbury, H., Murray, S.T., Swart, P.K., 2018. Mineralogy, early marine diagenesis, and the chemistry of shallow-water carbonate sediments. *Geochim. Cosmochim. Acta.* 220, 512–534.
- Higgins, J.A., Schrag, D.P., 2015. The Mg isotopic composition of Cenozoic seawater – evidence for a link between Mg-clays, seawater Mg/Ca, and climate. *Earth. Planet. Sci. Lett.* 416, 73–81.
- Hood, A.V.S., Wallace, M.W., 2012. Synsedimentary diagenesis in a Cryogenian reef complex: Ubiquitous marine dolomite precipitation. *Sediment. Geol.* 255–256, 56–71.
- Hood, A.V.S., Wallace, M.W., 2014. Marine cements reveal the structure of an anoxic, ferruginous Neoproterozoic ocean. *J. Geol. Soc.* 171 (6), 741–744.
- Hood, A.V.S., Wallace, M.W., 2018. Neoproterozoic marine carbonates and their paleoceanographic significance. *Glob. Planet. Change* 160, 28–45.
- Hood, A.V.S., Wallace, M.W., Drysdale, R.N., 2011. Neoproterozoic aragonite-dolomite seas? Widespread marine dolomite precipitation in Cryogenian reef complexes. *Geology* 39 (9), 871–874.
- Horita, J., Zimmermann, H., Holland, H.D., 2002. Chemical evolution of seawater during the Phanerozoic: Implications from the record of marine evaporites. *Geochim. Cosmochim. Acta.* 66 (21), 3733–3756.

- Hu, Y., Cai, C., Liu, D., Pederson, C.L., Jiang, L., Shen, A., Immenhauser, A., 2020. Formation, diagenesis and palaeoenvironmental significance of upper Ediacaran fibrous dolomite cements. *Sedimentology* 67 (2), 1161–1187.
- Hu, Z., Hu, W., Liu, C., Sun, F., Liu, Y., Li, W., 2019. Conservative behavior of Mg isotopes in massive dolostones: From diagenesis to hydrothermal reworking. *Sedimentary Geology* 381, 65–75.
- Hu, Z., Hu, W., Wang, X., Lu, Y., Wang, L., Liao, Z., Li, W., 2017. Resetting of Mg isotopes between calcite and dolomite during burial metamorphism: Outlook of Mg isotopes as geothermometer and seawater proxy. *Geochim. Cosmochim. Acta.* 208, 24–40.
- Hua, H., Pratt, B.R., Zhang, L.-Y., 2003. Borings in Cloudina Shells: Complex Predator–Prey Dynamics in the Terminal Neoproterozoic. *Palaeos* 18 (4–5), 454–459.
- Huang, K.-J., Teng, F.-Z., Plank, T., Staudigel, H., Hu, Y., Bao, Z.-Y., 2018. Magnesium isotopic composition of altered oceanic crust and the global Mg cycle. *Geochim. Cosmochim. Acta.* 238, 357–373.
- Jiang, G., Shi, X., Zhang, S., Wang, Y., Xiao, S., 2011. Stratigraphy and paleogeography of the Ediacaran Doushantuo Formation (ca. 635–551 Ma) in South China. *Gondwana Res.* 19 (4), 831–849.
- Kasemann, S.A., Pogge von Strandmann, P.A.E., Prave, A.R., Fallick, A.E., Elliott, T., Hoffmann, K.-H., 2014. Continental weathering following a Cryogenian glaciation: Evidence from calcium and magnesium isotopes. *Earth. Planet. Sci. Lett.* 396, 66–77.
- Kaufman, A.J., Knoll, A.H., 1995. Neoproterozoic variations in the C-isotopic composition of seawater: stratigraphic and biogeochemical implications. *Precambr. Res.* 73 (1), 27–49.
- Knoll, A.H., 2003. Biomineralization and Evolutionary History. *Rev. Mineral. Geochem.* 54 (1), 329–356.
- Lawrence, M.G., Greig, A., Collerson, K.D., Kamber, B.S., 2006. Rare Earth Element and Yttrium Variability in South East Queensland Waterways. *Aquat. Geochem.* 12 (1), 39–72.
- Li, F., Webb, G.E., Algeo, T.J., Kershaw, S., Lu, C., Oehlert, A.M., Gong, Q., Pourmand, A., Tan, X., 2019a. Modern carbonate ooids preserve ambient aqueous REE signatures. *Chem. Geol.* 509, 163–177.
- Li, M., Wignall, P.B., Dai, X., Hu, M., Song, H., 2021. Phanerozoic variation in dolomite abundance linked to oceanic anoxia. *Geology* 49 (6), 698–702.
- Li, W., Beard, B.L., Li, C., Xu, H., Johnson, C.M., 2015. Experimental calibration of Mg isotope fractionation between dolomite and aqueous solution and its geological implications. *Geochim. Cosmochim. Acta.* 157, 164–181.
- Li, W., Bialik, O.M., Wang, X., Yang, T., Hu, Z., Huang, Q., Zhao, S., Waldmann, N.D., 2019b. Effects of early diagenesis on Mg isotopes in dolomite: The roles of Mn(IV)-reduction and recrystallization. *Geochim. Cosmochim. Acta.* 250, 1–17.
- Li, Z.-X., Evans, D.A.D., Halverson, G.P., 2013. Neoproterozoic glaciations in a revised global palaeogeography from the breakup of Rodinia to the assembly of Gondwanaland. *Sediment. Geol.* 294, 219–232.
- Lian, C., Ren, G., Qu, F., Tan, X., Li, L., Zeng, W., Hu, G., Liu, H., 2017. Review and prospect on the botryoidal structures from the Sinian Dengying Formation, Sichuan Basin, China. *Petroleum.* 3 (2), 190–196.
- Ling, H.-F., Chen, X., Li, D.A., Wang, D., Shields-Zhou, G.A., Zhu, M., 2013. Cerium anomaly variations in Ediacaran–earliest Cambrian carbonates from the Yangtze Gorges area, South China: implications for oxygenation of coeval shallow seawater. *Precambr. Res.* 225, 110–127.
- Ling, M.-X., Fatemeh, S., Fang-Zhen, T., Phillip D. H., Josiah, S. and Weidong, S., 2011. Homogeneous magnesium isotopic composition of seawater: an excellent geostandard for Mg isotope analysis. *Rapid Commun. Mass Spectrom.* 25(19), 2828–2836.
- Linnemann, U., Ovtcharova, M., Schaltegger, U., Gärtner, A., Hautmann, M., Geyer, G., Vickers-Rich, P., Rich, T., Plessen, B., Hofmann, M., Zieger, J., Krause, R., Kriesfeld, L., Smith, J., 2019. New high-resolution age data from the Ediacaran–Cambrian boundary indicate rapid, ecologically driven onset of the Cambrian explosion. *Terra Nova.* 31 (1), 49–58.
- Liu, C., Wang, Z., Macdonald, F.A., 2018. Sr and Mg isotope geochemistry of the basal Ediacaran cap limestone sequence of Mongolia: Implications for carbonate diagenesis, mixing of glacial meltwaters, and seawater chemistry in the aftermath of Snowball Earth. *Chem. Geol.* 491, 1–13.
- Liu, C., Wang, Z., Raub, T.D., Macdonald, F.A., Evans, D.A.D., 2014. Neoproterozoic cap-dolostone deposition in stratified glacial meltwater plume. *Earth. Planet. Sci. Lett.* 404, 22–32.
- Liu, Y., Hu, Z., Gao, S., Günther, D., Xu, J., Gao, C., Chen, H., 2008. In situ analysis of major and trace elements of anhydrous minerals by LA-ICP-MS without applying an internal standard. *Chem. Geol.* 257 (1), 34–43.
- Lowenstein, T.K., Timofeeff, M.N., Brennan, S.T., Hardie, L.A., Demicco, R.V., 2001. Oscillations in Phanerozoic seawater chemistry: evidence from fluid inclusions. *Science* 294 (5544), 1086–1088.
- Mavromatis, V., Meister, P., Oelkers, E.H., 2014. Using stable Mg isotopes to distinguish dolomite formation mechanisms: A case study from the Peru Margin. *Chem. Geol.* 385, 84–91.
- McLennan, S.M., 1989. Rare Earth Elements in sedimentary rocks: influence of provenance and sedimentary processes. *Geochemistry and Mineralogy of Rare Earth Elements*, In Bruce R. Lipin, G.A. McKay (Eds.) 169–120.
- Moffett, J.W., 1994. A radiotracer study of cerium and manganese uptake onto suspended particles in Chesapeake Bay. *Geochim. Cosmochim. Acta.* 58 (2), 695–703.
- Murdock, D.J.E., 2020. The ‘biomineralization toolkit’ and the origin of animal skeletons. *Biol. Rev.* 95 (5), 1372–1392.
- Nothdurft, L.D., Webb, G.E., Kamber, B.S., 2004. Rare earth element geochemistry of Late Devonian reefal carbonates, Canning Basin, Western Australia: confirmation of a seawater REE proxy in ancient limestones. *Geochim. Cosmochim. Acta* 68 (2), 263–283.
- Paula-Santos, G.M., Caetano-Filho, S., Enzweiler, J., Navarro, M.S., Babinski, M., Guacaneme, C., Kuchenbecker, M., Reis, H., Trindade, R.I.F., 2020. Rare earth elements in the terminal Ediacaran Bambui Group carbonate rocks (Brazil): evidence for high seawater alkalinity during rise of early animals. *Precambr. Res.* 336, 105506.
- Peters, S.E., Gaines, R.R., 2012. Formation of the ‘Great Unconformity’ as a trigger for the Cambrian explosion. *Nature* 484 (7394), 363–366.
- Pokrovsky, B.G., Mavromatis, V., Pokrovsky, O.S., 2011. Co-variation of Mg and C isotopes in late Precambrian carbonates of the Siberian Platform: A new tool for tracing the change in weathering regime? *Chem. Geol.* 290 (1), 67–74.
- Ries, J.B., Pike, D.A., Pratt, L.M., Lyons, T.W., Grotzinger, J.P., 2009. Superheavy pyrite ( $\delta^{34}\text{S}_{\text{pyr}} > \delta^{34}\text{S}_{\text{CAS}}$ ) in the terminal Proterozoic Nama Group, southern Namibia: A consequence of low seawater sulfate at the dawn of animal life. *Geology* 37 (8), 743–746.
- Sandberg, P.A., 1983. An oscillating trend in Phanerozoic non-skeletal carbonate mineralogy. *Nature* 305, 19–22.
- Sawaki, Y., Ohno, T., Tahata, M., Komiya, T., Hirata, T., Maruyama, S., Windley, B.F., Han, J., Shu, D., Li, Y., 2010. The Ediacaran radiogenic Sr isotope excursion in the Doushantuo Formation in the Three Gorges area, South China. *Precambr. Res.* 176 (1), 46–64.
- Stammeier, J.A., Hippel, D., Nebel, O., Leis, A., Grengg, C., Mittermayr, F., Kasemann, S. A., Dietzel, M., 2019. Radiogenic Sr and Stable C and O Isotopes Across Precambrian–Cambrian Transition in Marine Carbonatic Phosphorites of Malyi Karatau (Kazakhstan)—Implications for Paleo-environmental Change. *Geochem. Geophys. Geosyst.* 20 (1), 3–23.
- Stammeier, J.A., Hippel, D., Nebel, O., Dietzel, M., 2020. Magnesium isotope evidence for enhanced crustal reworking in lowermost Cambrian sedimentary rocks (Kazakhstan). *Palaeogeogr. Palaeoclimatol. Palaeoecol.* 538, 109452.
- Stanley, S.M., Hardie, L.A., 1998. Secular oscillations in the carbonate mineralogy of reef-building and sediment-producing organisms driven by tectonically forced shifts in seawater chemistry. *Palaeogeogr. Palaeoclimatol. Palaeoecol.* 144 (1), 3–19.
- Swart, P.K., 2015. The geochemistry of carbonate diagenesis: The past, present and future. *Sedimentology* 62 (5), 1233–1304.
- Teng, F.Z., Li, W.Y., Ke, S., Yang, W., Liu, S.A., Sedaghatpour, F., Wang, S.J., Huang, K.J., Hu, Y., Ling, M.X., 2015. Magnesium Isotopic Compositions of International Geological Reference Materials. *Geo. Geoanal. Res.* 39 (3), 329–339.
- Tipper, E.T., Galy, A., Gaillardet, J., Bickle, M.J., Elderfield, H., Carder, E.A., 2006. The magnesium isotope budget of the modern ocean: Constraints from riverine magnesium isotope ratios. *Earth. Planet. Sci. Lett.* 250 (1), 241–253.
- Tostevin, R., Shields, G.A., Tarbuck, G.M., He, T., Clarkson, M.O., Wood, R.A., 2016. Effective use of cerium anomalies as a redox proxy in carbonate-dominated marine settings. *Chem. Geol.* 438, 146–162.
- Tucker, M.E., 1982. Precambrian dolomites: Petrographic and isotopic evidence that they differ from Phanerozoic dolomites. *Geology* 10 (1), 7–12.
- Wang, J., He, Z., Zhu, D., Liu, Q., Ding, Q., Li, S., Zhang, D., 2020. Petrological and geochemical characteristics of the botryoidal dolomite of Dengying Formation in the Yangtze Craton, South China: Constraints on terminal Ediacaran “dolomite seas”. *Sediment. Geol.* 406, 105722.
- Wilkinson, B.H., Algeo, T.J., 1989. Sedimentary carbonate record of calcium-magnesium cycling. *Am. J. Sci.* 289 (10), 1158–1194.
- Wood, R., 2018. Exploring the drivers of early biomineralization. *Emerg. Top. Life. Sci.* 2 (2), 201–212.
- Wood, R., Ivantsov Andrey, Y., Zhuravlev Andrey, Y., 2017a. First macrobiota biomineralization was environmentally triggered. *Proc. R. Soc. London, Ser. B* 284 (1851), 20170059.
- Wood, R.A., Zhuravlev, A.Y., Sukhov, S.S., Zhu, M., Zhao, F., 2017b. Demise of Ediacaran dolomitic seas marks widespread biomineralization on the Siberian Platform. *Geology* 45 (1), 27–30.
- Xiao, S., Narbonne, G.M., Zhou, C., Laflamme, M., Grazhdankin, D.V., Moczydlowska-Vidal, M., Cui, H., 2016. Towards an Ediacaran time scale: Problems, protocols, and prospects. *Episodes* 39, 540–555.
- Yao, J., Cawood, P.A., Zhao, G., Han, Y., Xia, X., Liu, Q., Wang, P., 2021. Mariana-type ophiolites constrain the establishment of modern plate tectonic regime during Gondwana assembly. *Nat. Commun.* 12, 4189.
- Zhang, P., Hua, H., Liu, W., 2014. Isotopic and REE evidence for the paleoenvironmental evolution of the late Ediacaran Dengying Section, Ningqiang of Shaanxi Province, China. *Precambr. Res.* 242, 96–111.
- Zhang, G., Chen, D., Huang, K.-J., Liu, M., Huang, T., Yeasmin, R., Fu, Y., 2021. Dramatic attenuation of continental weathering during the Ediacaran–Cambrian transition: Implications for the climatic-oceanic-biological co-evolution. *Glob. Planet. Change* 203, 103518.
- Zhao, D., Hu, G., Wang, L., Li, F., Tan, X., She, M., Zhang, W., Qiao, Z., Wang, X., 2020. Sedimentary characteristics and origin of dolomitic ooids of the terminal Ediacaran Dengying Formation at Yulin (Chongqing, South China). *Palaeogeogr. Palaeoclimatol. Palaeoecol.* 544, 109601.
- Zhao, D., Tan, X., Hu, G., Wang, L., Wang, X., Qiao, Z., Luo, S., Tang, H., 2021. Characteristics and primary mineralogy of fibrous marine dolomite cements in the end-Ediacaran Dengying Formation, South China: Implications for aragonite–dolomite seas. *Palaeogeogr. Palaeoclimatol. Palaeoecol.* 110635.
- Zhou, C., Yuan, X., Xiao, S., Chen, Z., Hua, H., 2019. Ediacaran integrative stratigraphy and timescale of China. *Sci. China: Earth Sci.* 62 (1), 7–24.
- Zhu, M., Zhang, J., Yang, A., 2007. Integrated Ediacaran (Sinian) chronostratigraphy of South China. *Palaeogeogr. Palaeoclimatol. Palaeoecol.* 254 (1), 7–61.